

Variability of Sea Level and Upper-Ocean Heat Content in the Indian Ocean: Effects of Subtropical Indian Ocean Dipole and ENSO[©]

LEI ZHANG, WEIQING HAN, YUANLONG LI, AND NICOLE S. LOVENDUSKI

Department of Atmospheric and Oceanic Sciences, University of Colorado, Boulder, Colorado

(Manuscript received 1 March 2019, in final form 28 July 2019)

ABSTRACT

In this study, the Indian Ocean upper-ocean variability associated with the subtropical Indian Ocean dipole (SIOD) is investigated. We find that the SIOD is associated with a prominent southwest–northeast sea level anomaly (SLA) dipole over the western-central south Indian Ocean, with the north pole located in the Seychelles–Chagos thermocline ridge (SCTR) and the south pole at southeast of Madagascar, which is different from the distribution of the sea surface temperature anomaly (SSTA). While the thermocline depth and upper-ocean heat content anomalies mirror SLAs, the air–sea CO₂ flux anomalies associated with SIOD are controlled by SSTA. In the SCTR region, the westward propagation of oceanic Rossby waves generated by anomalous winds over the eastern tropical Indian Ocean is the major cause for the SLAs, with cyclonic wind causing negative SLAs during positive SIOD (pSIOD). Local wind forcing is the primary driver for the SLAs southeast of Madagascar, with anticyclonic winds causing positive SLAs. Since the SIOD is correlated with ENSO, the relative roles of the SIOD and ENSO are examined. We find that while ENSO can induce significant SLAs in the SCTR region through an atmospheric bridge, it has negligible impact on the SLA to the southeast of Madagascar. By contrast, the SIOD with ENSO influence removed is associated with an opposite SLA in the SCTR and southeast of Madagascar, corresponding to the SLA dipole identified above. A new subtropical dipole mode index (SDMI) is proposed, which is uncorrelated with ENSO and thus better represents the pure SIOD effect.

1. Introduction

Sea level variability and change affect millions of people living in the coastal regions and island nations, and thus have large impact on human society (Stammer et al. 2013; Kopp et al. 2015; Han et al. 2017). Observational analyses have shown that the Indian Ocean sea level exhibits interannual-to-decadal variability and large regional differences, which differ significantly from the global mean and are largely attributable to the natural internal climate modes [see reviews by Stammer et al. (2013) and Han et al. (2017, 2019), and references therein].

As the dominant mode of the tropical Pacific climate variability, El Niño–Southern Oscillation (ENSO; Bjerknes 1969; Cane et al. 1986; Philander 1990) is

associated with significant sea level anomalies (SLAs) not only in the Pacific but also over the Indian Ocean from interannual to multidecadal time scales [e.g., Frankcombe et al. 2015; Li and Han 2015; Sayantani and Gnanaseelan 2015; Nidheesh et al. 2017; Deepa et al. 2018; Deepa et al. 2019; see also the reviews by Han et al. (2017, 2019) and references therein]. During La Niña, easterly wind anomalies over the equatorial Pacific induce prominent positive SLAs in the western equatorial Pacific, which influence the Indonesian Throughflow (ITF) and thus affect the SLAs in the tropical Indian Ocean (Clarke and Liu 1994; Meyers 1996; Masumoto and Meyers 1998; Feng et al. 2004; Wijffels and Meyers 2004; Clarke and Li 2004). In addition to this oceanic connection via the ITF, ENSO also affects the Indian Ocean SLAs via the atmospheric bridge by causing surface wind anomalies over the Indian Ocean. La Niña drives cyclonic wind anomalies centered at the southeast Indian Ocean, and the associated northerly wind anomalies along the Australian west coast cause higher sea level by causing anomalous coastal downwelling (Feng et al. 2013; Zhang et al. 2018). The evident higher

[©] Supplemental information related to this paper is available at the Journals Online website: <https://doi.org/10.1175/JCLI-D-19-0167.s1>.

Corresponding author: Lei Zhang, lezh8230@colorado.edu

coastal sea level anomalies are closely related to the Ningaloo Niño events (Feng et al. 2013; Zhang et al. 2018; Zhang and Han 2018), a climate phenomenon that depicts marine heatwave events off the west coast of Australia (Feng et al. 2013). Over the south Indian Ocean interior, the ENSO-related surface wind anomalies also cause large-amplitude SLAs and upper-ocean heat content variability in the Seychelles–Chagos thermocline ridge (SCTR) region (Masumoto and Meyers 1998; Xie et al. 2002; Trenary and Han 2013; Han et al. 2014; Huang and Kinter 2002).

In addition to ENSO, the Indian Ocean SLAs are also strongly affected by the Indian Ocean dipole (IOD), a coupled ocean–atmosphere mode of climate variability over the tropical Indian Ocean (Saji et al. 1999; Webster et al. 1999), which is correlated with ENSO but sometimes can occur independently from ENSO (Iizuka et al. 2000; Saji and Yamagata 2003; Shinoda et al. 2004; Yang et al. 2015). During the positive phase of the IOD, the cold sea surface temperature anomalies (SSTAs) in the eastern tropical Indian Ocean and the warm SSTAs in the west induce surface easterly wind anomalies, which subsequently cause negative SLA in the eastern basin and positive SLA in the western basin (Feng et al. 2001; Rao et al. 2002; Gualdi et al. 2003; Frankcombe et al. 2015). On decadal time scale, Indian Ocean sea level variability associated with the decadal variability of ENSO, IOD, and Indian summer monsoon has been examined recently (Han et al. 2018).

Despite our progress in understanding the regional sea level variability in the Indian Ocean and its association with climate modes, the SLA pattern associated with the subtropical Indian Ocean dipole (SIOD) mode (Behera and Yamagata 2001) remains unknown. The SIOD is another climate mode associated with large-scale wind and SST anomalies in the subtropical south Indian Ocean, with negative SSTA occurring in the southeast Indian Ocean basin and positive SSTA occurring in the western basin southeast of Madagascar during its positive phase (Behera and Yamagata 2001; Suzuki et al. 2004; Chiodi and Harrison 2007; Morioka et al. 2010). The SIOD is phase-locked to the seasonal cycle, usually developing during December–January, peaking in February–March, and decaying during April–May (Behera and Yamagata 2001). Although a recent study speculated that decadal variability of the SIOD may have contributed to the surface wind variation over the equatorial Indian Ocean, which drove the cross-equatorial heat transport and thus decadal sea level variation of the north Indian Ocean in recent decades (Thompson et al. 2016), the relationship between the SIOD and the Indian Ocean SLA and surface wind fields has not yet been elucidated.

Upper ocean variability associated with the SIOD (e.g., temperature, upwelling) may also affect local biogeochemical processes. Recent efforts to observe the biogeochemistry of the Indian Ocean [e.g., the ongoing Second International Indian Ocean Expedition (IIOE-2) program; <https://iioe-2.incois.gov.in>] have renewed interest in quantifying and understanding spatial and temporal variability in Indian Ocean biogeochemical processes. To this end, a simple investigation of the relationship between the interannually varying SIOD and air-sea CO_2 flux would continue to evolve our understanding of this important quantity beyond the seasonal cycle (Poisson et al. 1993; Metzl et al. 1995; Sabine et al. 2000; Bates et al. 2006).

In this study, we investigate the connection between the SIOD and the Indian Ocean SLAs and upper-ocean heat content (UOHC) using both observational analyses and ocean general circulation model (OGCM) experiments. Since the SIOD is correlated with ENSO (Hermes and Reason 2005), we will also examine the effect of ENSO, and assess the relative contributions of ENSO and SIOD to the upper-ocean variations in the south Indian Ocean, where evident SIOD impacts are found, as we shall see in section 3 below. Understanding the impacts of natural internal climate modes on regional sea level is not only a prerequisite for anthropogenic fingerprints being identified, but also essential for sea level prediction, because the predictability of climate modes implies predictability of regional sea level change. The rest of the paper is organized as follows. Section 2 provides detailed descriptions of model and data used in this study. Section 3 characterizes SLAs associated with the SIOD and explores their physical causes. Section 4 discusses the relative contributions of ENSO and SIOD to the SLAs in the south Indian Ocean. Section 5 summarizes the results.

2. Data and model

a. Observations

To document the variability of sea level, SST, and UOHC, we analyze monthly SST data from the Hadley Centre Sea Ice and Sea Surface Temperature dataset (HadISST; Rayner et al. 2003) and monthly sea level and ocean temperature data from European Centre for Medium-Range Weather Forecasts (ECMWF) Ocean Reanalysis System 4 (ORAS4; Balmaseda et al. 2013a,b) for the period 1958–2016. In this study, we define the depth of the 20°C isotherm (D20) as the thermocline depth. To examine the role of surface winds in causing sea level and upper-ocean variability (e.g., SST and UOHC), we also analyze surface wind fields from the ECMWF Twentieth Century Reanalysis (ERA-20C;

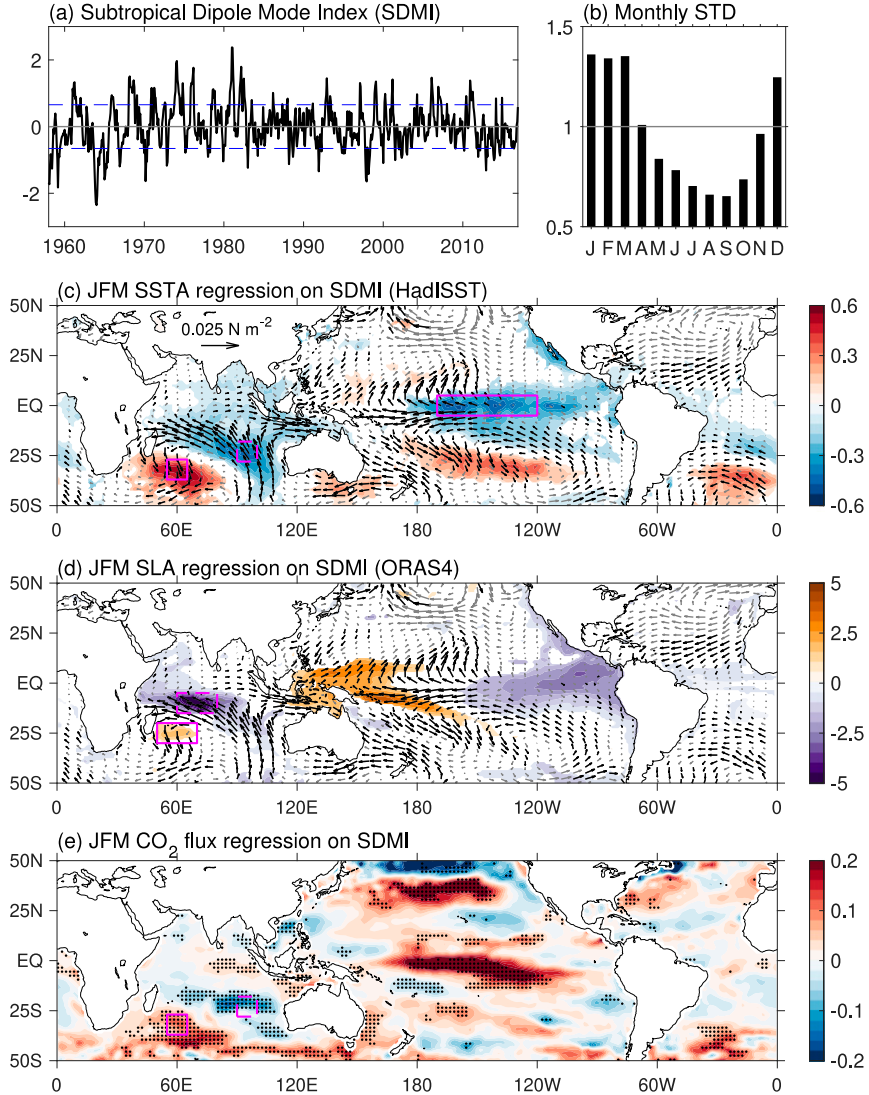


FIG. 1. (a) Time evolution of the SDMI ($^{\circ}\text{C}$) from 1958 to 2016, defined as differences of SSTA averaged over 55° – 65°E , 37° – 27°S and 90° – 100°E , 28° – 18°S [boxed region in (c)], following Behera and Yamagata (2001). HadISST data are used for calculating the SSTA. The dashed blue line denotes the one standard deviation (STD) of the SDMI. (b) Monthly STD of the normalized SDMI. (c) Shading denotes regression of JFM mean SSTA ($^{\circ}\text{C}$) on the normalized JFM SDMI, and vectors denote regression of the JFM surface wind stress from ERA-20C and ERA-Interim (N m^{-2}). The box in the tropical Pacific denotes the Niño-3.4 region. (d) As in (c), but for regression of JFM SLA (cm) using ORAS4 reanalysis data. Boxes in the Indian Ocean denote the SLA dipole regions (60° – 80°E , 15° – 5°S and 50° – 70°E , 30° – 20°S). (e) As in (c), but for JFM CO₂ flux density anomalies ($\text{mol m}^{-2} \text{yr}^{-1}$). Shading and black vectors in (c) and (d) and stippling in (e) denote results that are statistically significant at the 90% confidence level.

Poli et al. 2016) available for 1958–2010, and the ERA-Interim reanalysis for 2011–16 (Dee et al. 2011). Satellite-derived sea level data from Archiving, Validation, and Interpretation of Satellite Oceanographic (AVISO; Ducet et al. 2000) and SST data from National Oceanic and Atmospheric Administration (NOAA) Optimum Interpolation SST v2 (OISST; Reynolds et al. 2002) are also analyzed for comparisons. To analyze the

impact of SIOD on air-sea CO₂ flux variability in the Indian Ocean, an observation-based air-sea CO₂ flux product over 1982–2011 is analyzed (Landschützer et al. 2014).

Following Behera and Yamagata (2001), we define the subtropical dipole mode index (SDMI) as differences of SSTA averaged over the domains 55° – 65°E , 37° – 27°S and 90° – 100°E , 28° – 18°S (Fig. 1c), used to

represent the SIOD evolution. Linear regressions of different variables on the SDMI are calculated to characterize the large-scale patterns associated with the SIOD, and therefore both the positive and negative phases of the SIOD have been taken into consideration. In this study, we refer to the latitudes south of 15°S as subtropics and from north of 15°S to the equator as tropics, because 15°S is the latitude where the long-term mean Ekman pumping is approximately zero, which separates the tropical upwelling from subtropical subduction (see Han et al. 2006; Trenary and Han 2008). To document ENSO variability, we calculated the Niño-3.4 index (170°–120°W, 5°S–5°N). We define the positive (negative) SIOD event as when the January–March (JFM) mean SDMI values exceed one positive (negative) standard deviation of the SDMI over the analysis period. Similarly, El Niño (La Niña) is defined as the November–January (NDJ) Niño-3.4 index exceeds one positive (negative) standard deviation of the Niño-3.4 index. The selected SIOD years are listed in Table S1 in the online supplemental material. All the anomalies of variables have been detrended in this study.

b. OGCM and experiments

To help quantify the relative roles of different physical processes in causing the upper Indian Ocean variability associated with the SIOD, we performed OGCM experiments using the Hybrid Coordinate Ocean Model version 2.2.18 (HYCOM; Bleck 2002). We configured HYCOM to the Indo-Pacific Ocean basin over 19°E–68°W, 55°S–50°N. The zonal grid size is $\frac{1}{3}^{\circ}$ between 70°–170°E and gradually enlarges to 1° west of 40°E and east of 160°W, while the meridional grid size is $\frac{1}{3}^{\circ}$ at low latitudes (25°S–25°N) and enlarges to 1° at midlatitudes poleward of 44° (Fig. S1). The higher horizontal resolution may help to improve the simulation of the oceanic interbasin processes (e.g., the ITF), although as shown below it does not completely cover the region where the strongest SLAs associated with the SIOD are located. The model has 35 hybrid vertical layers, with a top layer thickness of 5 m. The spinup time is 30 years, and then the model was integrated forward in time from 1940 to 2010, using daily ERA-20C fields as the surface atmospheric forcing. The HYCOM results of 1958–2010 were used for our analysis, to be consistent with the observational analyses.

In the main run (HYCOM_MR) experiment, we forced the model using full daily forcing fields of ERA-20C over the entire Indo-Pacific region. This is the complete solution in the suite of HYCOM experiments, and its results were compared with the observations. To investigate the Pacific impacts on the Indian Ocean through the oceanic connection (ITF effect), we used

full forcing in the Pacific Ocean, while the forcing over the Indian Ocean only contains climatological seasonal cycle. As such, variability of the Indian Ocean sea level in this experiment is predominantly caused by the ITF variability dictated by the Pacific climate, and therefore this experiment is named HYCOM_ITF. An additional experiment (HYCOM_TAU) is also performed, using full daily surface wind stress forcing over both the Indian and Pacific Oceans, while other forcing fields are fixed to monthly climatology. Note that the ITF impact is also included in HYCOM_TAU, since its variability is largely driven by surface wind stress anomalies over the tropical Pacific (Li et al. 2017, 2018). Hence, the difference between the two experiments, HYCOM_TAU – HYCOM_ITF, isolates the impacts of the Indian Ocean surface wind stress anomalies. Further, HYCOM_MR – HYCOM_TAU assesses effects of other forcing fields, including surface heat and freshwater fluxes.

3. SLA associated with the SIOD

a. Observational analyses: Characteristics

The SIOD is the dominant interannual SST variability mode of the subtropical south Indian Ocean. The SDMI, which depicts the temporal evolution of the SIOD, shows significant variability on interannual time scales (Fig. 1a). Analysis of monthly standard deviation of the observed SDMI shows that the SIOD peaks in the January–March austral summer season (Fig. 1b), consistent with Behera and Yamagata (2001). During its mature phase, the positive SIOD (pSIOD) is characterized by warm SSTA centered in the region southeast of Madagascar and cold SSTA centered at the southeast Indian Ocean basin, accompanied by large-scale anticyclonic wind anomalies over the entire south Indian Ocean (Fig. 1c), suggesting a strengthened Mascarene high (Fig. S2).

While the SLA pattern bears some resemblance to that of the SSTA, with negative SLA in the colder SSTA region and positive SLA in the warmer SSTA region, there are significant differences. In contrast to the SSTA, which primarily exhibits an east–west dipole structure, the SLA dipole is primarily oriented in the southwest–northeast direction and both poles are shifted to the western basin, with negative SLAs in the SCTR region accompanied by weak positive SLAs off the southeast coast of Madagascar during the pSIOD. Furthermore, the positive SLA maximum is located to the north of the warm SSTA maximum where SSTA is weak. These differences suggest that the physical processes that cause SLAs and SSTAs associated with the SIOD are different, which will be discussed in detail in the next section.

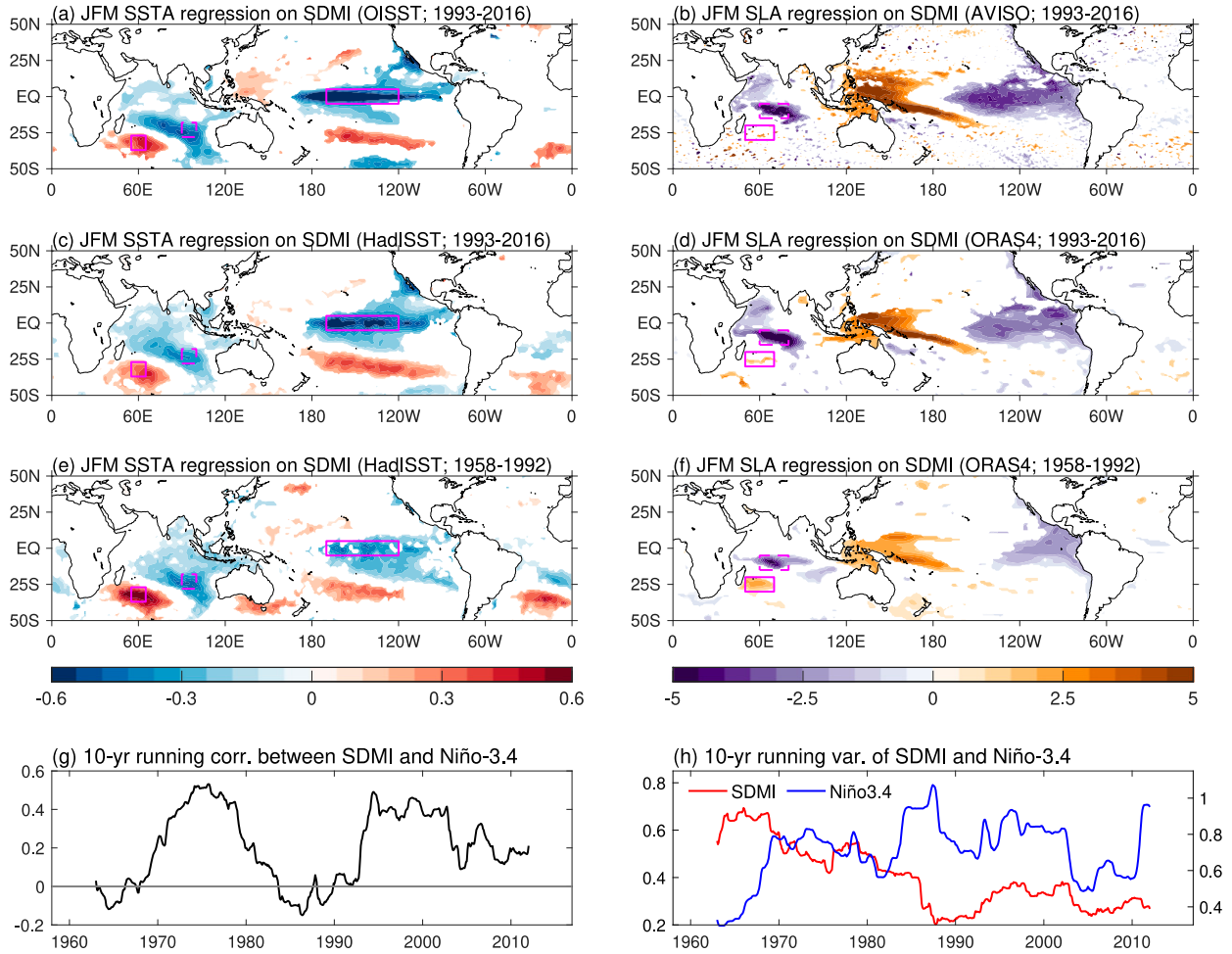


FIG. 2. (a) Regression of JFM mean SSTA ($^{\circ}$ C) on the normalized JFM SDMI using OISST during 1993–2016. (b) As in (a), but for regression of JFM SLA (cm) on SDMI using AVISO during 1993–2016. (c),(d) As in (a) and (b), but for results using HadISST and ORAS4 during 1993–2016. (e),(f) As in (a) and (b), but for results using HadISST and ORAS4 during 1958–92. Shown in (a)–(f) are results that are statistically significant at the 90% confidence level. (g) Time evolution of 10-yr running correlation between the SDMI and flipped Niño-3.4 index. (h) Time evolution of 10-yr running variance ($^{\circ}$ C 2) of the SDMI (red; left axis) and Niño-3.4 index (blue; right axis).

We also find that the SIOD is associated with prominent changes in the air-sea CO₂ flux in the south Indian Ocean. The spatial pattern of the CO₂ flux anomalies follows that of SSTA (Fig. 1e), with positive SSTA corresponding to more CO₂ release from the ocean surface. This result suggests that in the south Indian Ocean where the upper-ocean upwelling is generally weak, variability in the sea surface CO₂ concentration is primarily controlled by SST (solubility), while the ocean circulation only plays a minor role. This is in contrast with the enhanced CO₂ flux anomalies in the tropical Pacific in spite of the negative SSTA (Fig. 1e), which is due to the strengthened upwelling that brings cold, carbon-rich water to the surface.

In agreement with previous studies (e.g., [Hermes and Reason 2005](#)), the SIOD is related to ENSO with pSIOD corresponding to La Niña condition in the

tropical Pacific (Figs. 1c,d). During La Niña, deep convection is enhanced over the Maritime Continent, which excites damped Rossby waves manifested as cyclonic wind anomalies in the southeast Indian Ocean ([Gill 1980](#)). The associated southeasterly wind anomalies at the western edge could enhance the anticyclonic wind anomalies to their west during the pSIOD. Note that because the anomalies in Fig. 1c are primarily associated with the SIOD, the anomalous cyclone over the southeast Indian Ocean associated with the La Niña forcing is weak and less evident. Despite such connection with ENSO, as we shall see below, the pSIOD events are not always accompanied by La Niñas, and thus the SIOD can act independently from ENSO.

For comparison, we analyze the SLAs and SSTAs associated with the SIOD using satellite data during 1993–2016 (Figs. 2a,b), and the results show overall

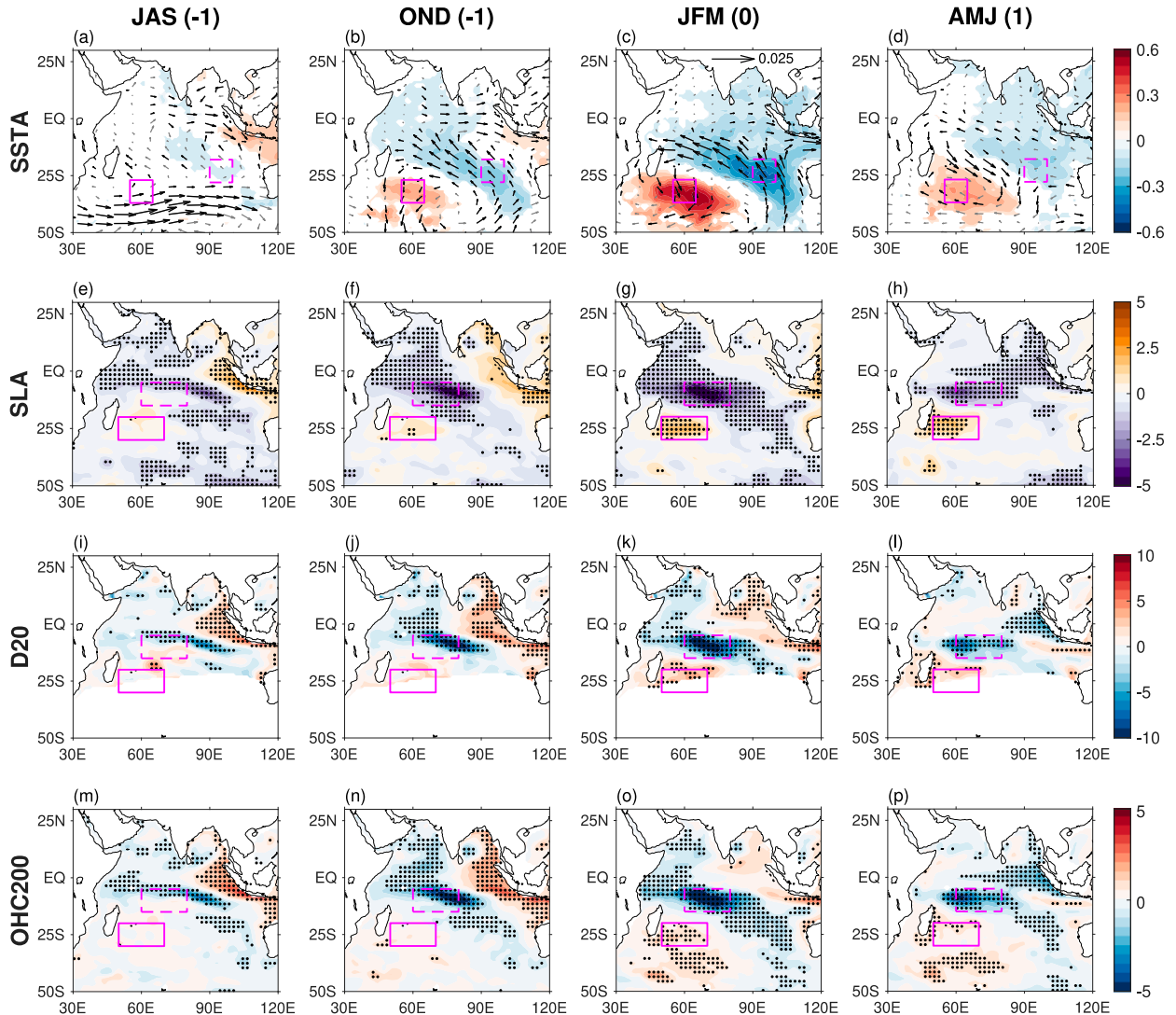


FIG. 3. (a) Regression of JAS SSTA ($^{\circ}\text{C}$) and surface wind stress (N m^{-2}) on the normalized JFM SDMI in the following year. (b) As in (a), but for regression of OND SSTA and surface wind stress on the normalized JFM SDMI in the following year. (c) As in (a), but for regression of JFM SSTA and surface wind stress on the normalized JFM SDMI. (d) As in (a), but for regression of AMJ SSTA and surface wind stress on the preceding normalized JFM SDMI. (e)–(h) As in (a)–(d), but for regression of SLA (cm). (i)–(l) As in (a)–(d), but for regression of D20A (m). (m)–(p) As in (a)–(d), but for regression of UOHC above 200 m (10^8 J m^{-2}). Shading and black vectors in (a)–(d) and stippling in (e)–(p) denote results that are statistically significant at the 90% confidence level. Note that to the south of 25°S, D20 outcrops and thus has no data.

similar patterns to those in our previous analyses for the period of 1958–2016, including the east–west SSTA dipole and north–south SLA dipole in the subtropical south Indian Ocean, and the La Niña condition in the tropical Pacific. However, the positive SLA pole to the southeast of Madagascar is much weaker in the satellite data. Analysis of HadISST and ORAS4 during 1993–2016 shows similar results (Figs. 2c,d). Prior to 1993, on the other hand, the SLA dipole in the southwest Indian Ocean during the pSIOD is well captured (Figs. 2e,f), suggesting apparent decadal variations of SIOD. Such

decadal variations of the SIOD-related SLAs seem related to the weakened strength of SIOD after late 1980s (Fig. 2h) and the prominent impact of ENSO on the subtropical south Indian Ocean (Fig. 2g). See section 4 for detailed examination of their relative roles.

b. Seasonal evolution

Given that the SIOD exhibits strong seasonality (Fig. 1b), here we examine the seasonal evolution of SSTA, SLA, thermocline depth (represented by D20) anomalies (D20A), and upper-ocean heat content

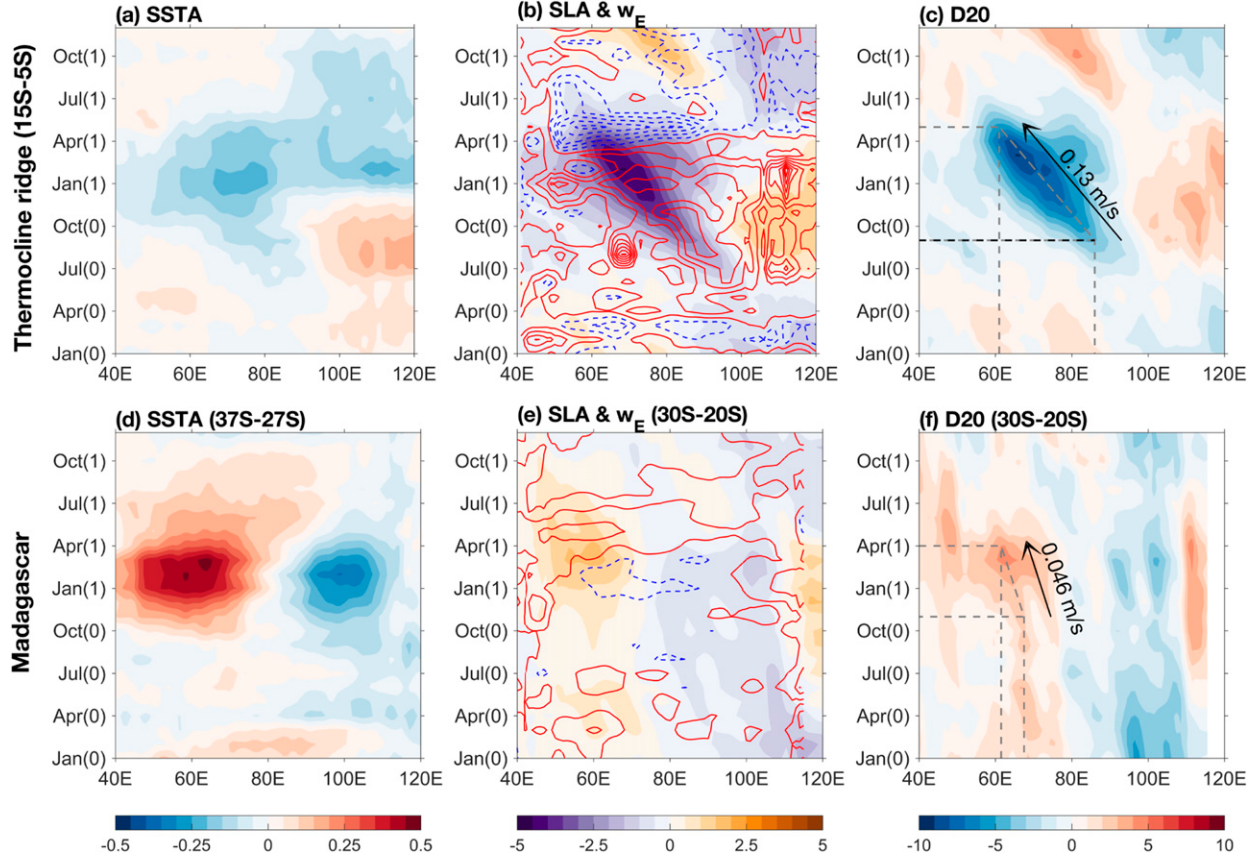


FIG. 4. (a) Lead-lag regression of SST ($^{\circ}\text{C}$) averaged over the latitudinal band $15^{\circ}\text{--}5^{\circ}\text{S}$ (the latitude range of the SLA SCTR box of Figs. 1–3) on the normalized JFM SDMI. (b) As in (a), but for regression of SLA (shading; cm) and the Ekman pumping velocity w_E anomalies (contours; 10^{-6} m s^{-1} ; contour interval $0.2 \times 10^{-6} \text{ m s}^{-1}$); $w_E = [\partial(\tau^y/\rho_o f)/\partial x] - [\partial(\tau^x/\rho_o f)/\partial y]$, where ρ_o is water density, f is the Coriolis parameter, and (τ^x, τ^y) are surface (zonal, meridional) wind stress. Blue contours denote negative values and red for positive values. (c) As in (a), but for regression of D20A (m). The black arrow denotes the westward propagation of D20A, the speed of which is estimated at approximately 0.13 m s^{-1} . Dashed gray lines mark the time and longitude used to estimate the phase speed. (d)–(f) As in (a)–(c), but for variables averaged over the latitudinal band $37^{\circ}\text{--}27^{\circ}\text{S}$ (covers the west SSTA box in Figs. 1–3) in (d) and $30^{\circ}\text{--}20^{\circ}\text{S}$ in (e) and (f).

anomalies (UOHCAs) associated with SIOD during its developing, mature, and decaying phases. The SSTA dipole and the associated anticyclonic wind anomalies in the subtropical south Indian Ocean start to appear during July–September (JAS), develop and intensify during October–December (OND), reach peaks during JFM and subsequently decay during April–June (AMJ), with no apparent propagation at all stages (Figs. 3a–d). Note that the eastern basin cold SSTA and southeasterly wind anomalies of pSID extend northwestward into the tropics, occupying the climatological mean SCTR region located north of the warm SSTA (Fig. S2).

The SLA dipole, on the other hand, exhibits remarkably different evolution patterns, even though the timings of development, peak, and decay agree with those of the SSTA (Figs. 3e–h). The SLAs in the SCTR region exhibit westward propagation, while the propagation of SLAs to the east of Madagascar is not as

apparent and at a much slower speed. The D20A, which agree with the variability of the UOHC, mirror SLAs very well in both SCTR and the subtropical south Indian Ocean, with a rising sea level corresponding to a deepening D20 and increasing UOHC (Figs. 3i–p), consistent with the dominant baroclinic response of the upper Indian Ocean to surface wind forcing (e.g., Fukumori et al. 1998).

To better illustrate the different propagating characteristics of the SSTA, SLA, and D20A associated with the SIOD, Fig. 4 shows their Hovmöller diagrams. In the subtropical south Indian Ocean ($37^{\circ}\text{--}27^{\circ}\text{S}$) where the largest SSTA associated with the SIOD is located, the SSTA dipole is indeed stationary, and only develops and decays locally (Fig. 4d). Meanwhile, SLA and D20A in the western basin over $30^{\circ}\text{--}20^{\circ}\text{S}$ show slow westward propagation (Figs. 4e,f). In the SCTR latitude band ($15^{\circ}\text{--}5^{\circ}\text{S}$), on the other hand, the SLA and the D20A

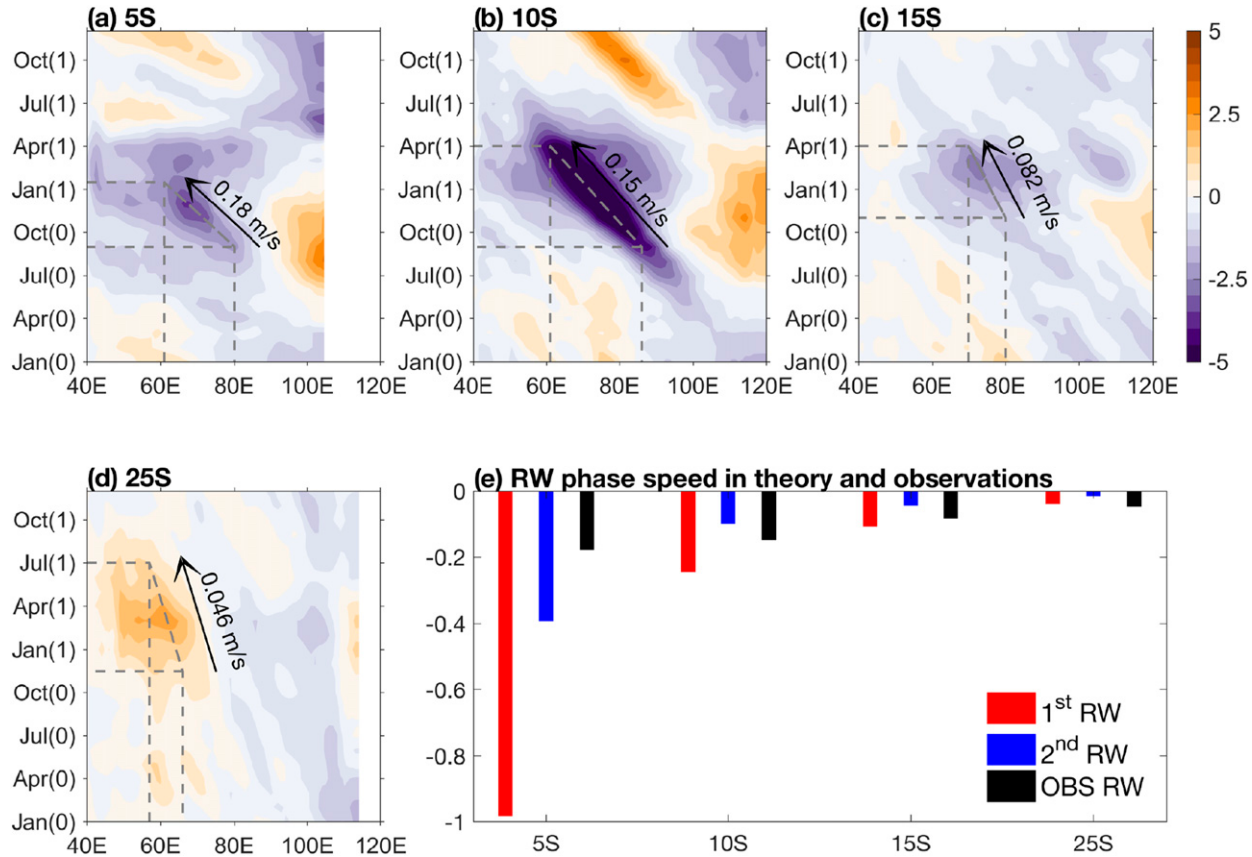


FIG. 5. (a) Lead-lag regression of SLA (cm) on the normalized JFM SDMI. (b)–(d) As in (a), but for SLA at 10°, 15°, and 25°S, respectively. Black arrows in (a)–(d) denote the westward propagation of SLA, the speed of which is shown in each panel. (e) The first (red) and second (blue) baroclinic Rossby wave speed c_r and the phase speed of the Rossby waves estimated in (a)–(d) (black) at different latitudes; c_r is obtained using the equation $c_r = -\beta c^2/f^2$, where f is the Coriolis parameter and $\beta = df/dy$, with the typical characteristic speeds of $c_1 = 2.64$ and $c_2 = 1.67 \text{ m s}^{-1}$.

associated with the SIOD propagate westward at a speed of approximately 0.13 m s^{-1} (Figs. 4b,c). By contrast, the cold SSTA does not show apparent propagation (Fig. 4a).

c. Physical mechanisms

Here, we examine the physical processes that cause the SLA dipole associated with the SIOD. As pointed out in previous studies, the observed westward propagation of interannual SLA signals along the SCTR latitude band results from oceanic Rossby waves, which are forced by surface winds from the east (Tozuka et al. 2010; Trenary and Han 2012). In the eastern basin of the south Indian Ocean, westward propagating interannual Rossby waves have also been shown by previous studies (Masumoto and Meyers 1998; Zhuang et al. 2013). Given that the phase speed of the baroclinic Rossby waves strongly depend on the latitude, $c_r = -\beta c^2/f^2$ (see caption of Fig. 5), we further analyze the zonal SLA propagation at 5°, 10°, and 15°S (Fig. 5). As expected, the

phase speed is slower at higher latitude. The westward propagation speed of SLA is ~ 0.18 , 0.15 , and 0.084 m s^{-1} at 5°, 10° and 15°S, respectively. It can also be seen that the SLAs and D20As at lower latitudes clearly lead those at higher latitudes over the 15°–5°S latitude band (Fig. 3). At 10° and 15°S, the observed phase speeds are between the first and second baroclinic Rossby wave phase speeds (Fig. 5e), suggesting that the observed Rossby waves are largely composed by the first two baroclinic modes, consistent with previous findings (Chambers et al. 1999; Trenary and Han 2013). At 5°S, the estimated phase speed is slower than the second baroclinic Rossby wave's speed, suggesting contributions from higher-order baroclinic modes. However, cautions are needed for interpreting these results. For instance, the estimated speed closer to mode 1 does not necessarily mean it is dominated by the contribution of mode 1. This is because the observed signals are not just free Rossby waves that propagate from the east; rather, they include local wind forcing and oceanic instabilities.

The negative SLA in the SCTR region is accompanied by positive w_E anomalies across the basin, which are associated with easterly and southeasterly wind anomalies at the northern flank of the anomalous anticyclone (Fig. 4b). The across basin positive w_E will enhance the SLA and D20A amplitudes associated with Rossby waves while they propagate westward, as shown by the good agreement between the zonal integral of w_E along Rossby waves' characteristics and the SLA/D20A magnitudes (Fig. 6). To the southeast of Madagascar (i.e., the south pole of the SLA dipole), SLAs are associated with negative w_E anomalies and also propagate westward at a speed that is close to the first baroclinic Rossby waves, even though the SLA and D20A signals are noisy due to oceanic instabilities in this latitude range (Figs. 4e, 5d, and 5e; Trenary and Han 2013; Li and Han 2015). Hence, it is clear that the wind-driven oceanic wave dynamics are critical for causing the SLA dipole associated with the SIOD.

To further shed light on the importance of surface wind stress (i.e., w_E) in SLA/D20A and surface heat fluxes in SSTA during the SIOD, we analyze the results from the hierarchy of HYCOM experiments. The HYCOM_MR, which is forced by full forcing fields, is first compared to observations to validate the model performance. As shown in Fig. 7a, both the observed SDMI and the SLA dipole index are well reproduced by the HYCOM_MR (Fig. 7a); the correlation coefficient between HYCOM_MR and observations is ~ 0.8 for the two indices. The observed large-scale features of the SIOD, including the east–west SSTA dipole and the southwest–northeast SLA dipole are also well captured by HYCOM_MR (Figs. 7b,c), although the positive SLA to the southeast of Madagascar is underestimated in HYCOM. In addition, the association of the pSIOD with the Pacific La Niña can also be clearly seen in the HYCOM_MR.

To assess the relative roles of different forcing and processes in causing the SLAs associated with the SIOD, we analyze HYCOM_ITF, HYCOM_TAU combined with the HYCOM_MR. In HYCOM_ITF, forcing fields over the Indian Ocean only contain climatological seasonal cycles; therefore, SLAs in this experiment mainly result from the remote Pacific forcing via the ITF. As shown in Fig. 8d, the Pacific La Niña condition during the pSIOD enhances the ITF and increases sea level in the southeast Indian Ocean. The positive SLAs however are primarily confined to the east basin north and northwest of Australia, where the local w_E anomalies induced by the cyclonic winds are positive during the peak season of the pSIOD (Fig. 4b). After the SIOD peak, the positive SLAs continue extending westward (Fig. 9a), but the associated SLAs are weak in the SCTR

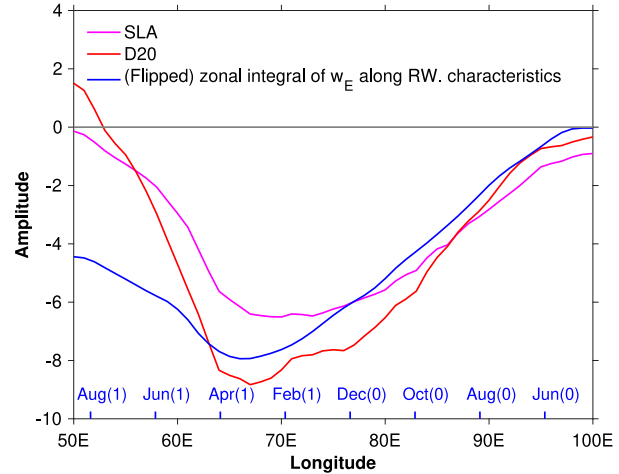


FIG. 6. The SLA (magenta; 2/3 cm) and D20A (red; m) along the Rossby wave characteristics at latitudes 15°–5°S, which are shown in Fig. 4c. The blue line denotes the zonal integral of w_E ($0.25 \text{ m}^2 \text{s}^{-1}$; flipped sign) to the east of Rossby waves starting from 100°E.

region and not in phase with the SLA dipole. Consequently, the remote forcing from the Pacific via the ITF does not affect the SLA dipole in the west-central Indian Ocean basin.

The difference between HYCOM_TAU and HYCOM_ITF, which isolates the effects of Indian Ocean surface wind stress anomalies, well captures the north–south SLA dipole associated with the SIOD (Fig. 8e). Furthermore, HYCOM_TAU–HYCOM_ITF also simulates the westward propagation of SLA in the SCTR (Fig. 9b), although its phase speed is faster than that in observations (0.21 vs 0.13 m s^{-1}). Such a difference could be due to the lack of forcing by surface heat fluxes and precipitation (Fig. 9c), which affect SSTA (Fig. 8c) and thus provide some feedbacks on surface heat fluxes, even though the effect of these factors is relatively weak (Fig. 9c). This “air–sea feedback” between SSTA and surface heat flux is included in HYCOM experiments, which could to some degree affect the Rossby wave propagation. In addition, salinity can directly affect SLA (Llovel and Lee 2015). At the south pole of the SLA dipole, the SLA signals propagate westward at a much slower speed (Fig. 9e), consistent with observations. These results show that the SIOD-related SLA dipole is primarily caused by the surface wind stress effect. During the pSIOD, the negative SLAs in the thermocline ridge region are associated with the cyclonic wind anomalies over the eastern tropical Indian Ocean and the subsequent westward propagation of oceanic Rossby waves; local wind forcing may further amplify those SLA. To the southeast of Madagascar, the positive SLAs are associated with the local anticyclonic

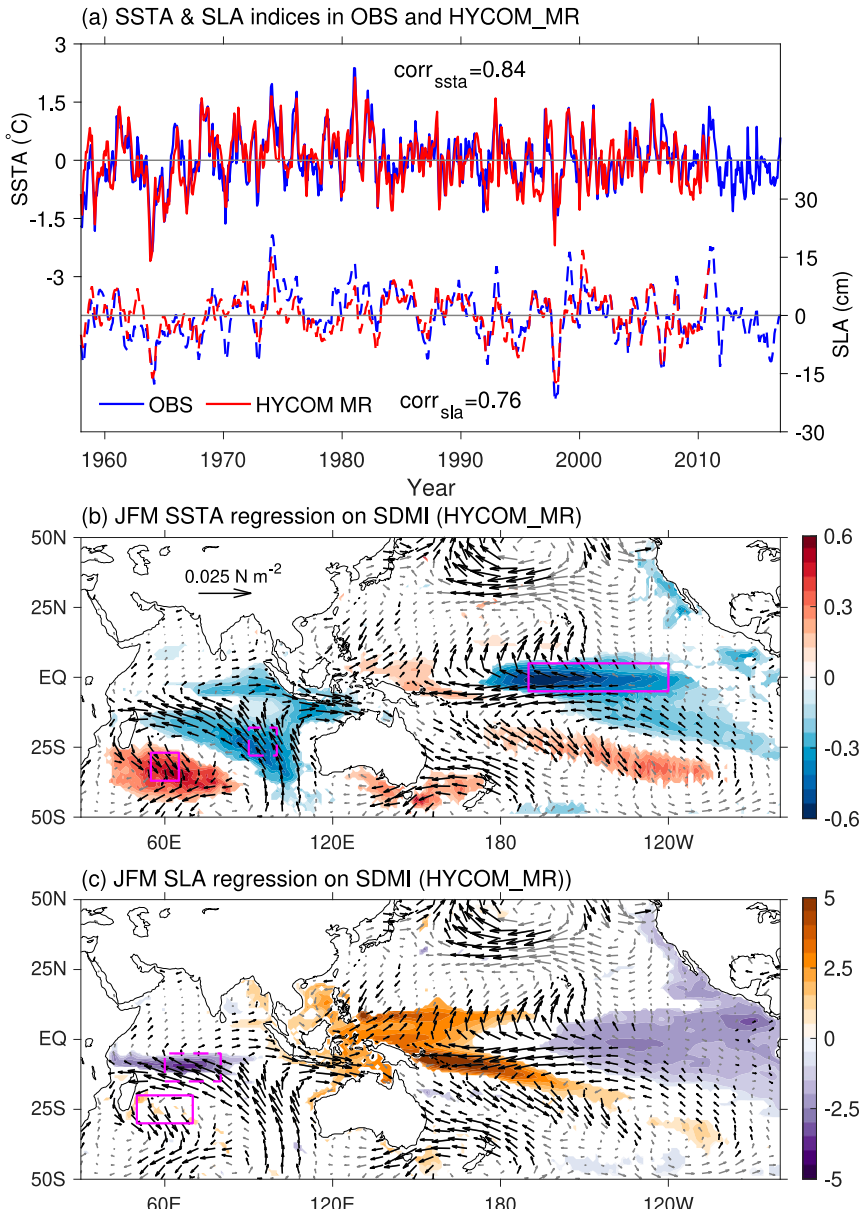


FIG. 7. (a) Time evolution of the SDMI ($^{\circ}$ C) and the SLA dipole index [cm; boxed regions in (c)]. Blue and red lines denote results from observations and HYCOM_MR, respectively, and correlation coefficients between the two are shown in the figure. (b) Results using HYCOM_MR. Shading denotes regression of JFM mean SSTA ($^{\circ}$ C) on the normalized JFM SDMI, and vectors denote regression of JFM surface wind stress ($N m^{-2}$). (c) As in (b), but for regression of JFM SLA (cm). Shading and black vectors in (b) and (c) denote results that are statistically significant at the 90% confidence level.

wind and negative w_E anomalies. Also note that the SLAs induced by the ITF and surface wind stress anomalies in the eastern tropical Indian Ocean are opposite and thus tend to partly cancel each other (Figs. 8d,e).

Different from the SLAs, the SIOD-associated SSTAs are mainly caused by surface heat flux anomalies

(Figs. 8a–c), with negligible contributions from the ITF and the surface wind stress forcing. These results support the aforementioned conclusion that SSTAs and SLAs associated with the SIOD are controlled by different physical processes, resulting in the different spatial patterns between the two (Figs. 1 and 3). Indeed, formation of the SSTA dipole has been attributed to

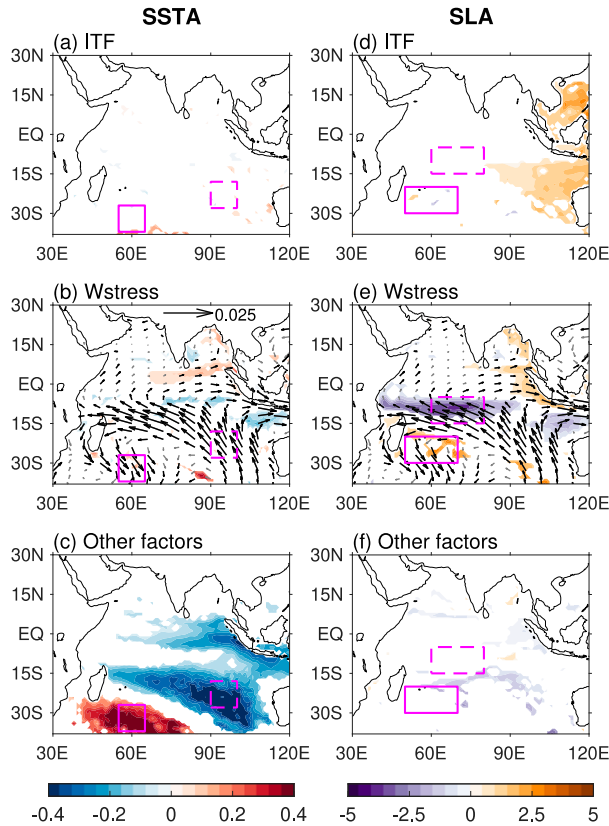


FIG. 8. (a) Regression of JFM SSTA in HYCOM_ITF (ITF effect) on the normalized JFM SDMI in HYCOM_MR ($^{\circ}\text{C}$). (b) As in (a), but for regression of SSTA in HYCOM_TAU – HYCOM_ITF (surface wind stress effect) and surface wind stress (N m^{-2}) on the normalized JFM SDMI in HYCOM_MR. (c) As in (a), but for regression of SSTA in HYCOM_MR – HYCOM_TAU (other factors). (d),(e) As in (a)–(c), but for regression of SLA (cm).

variations in surface latent heat fluxes due to wind changes and surface humidity changes by previous studies (Behera and Yamagata 2001; Suzuki et al. 2004; Chiodi and Harrison 2007), and surface solar radiation contributions related to mixed layer depth variations (Morioka et al. 2010). Our results agree with theirs on the forcing and processes of the SIOD-associated SSTA. Since this study mainly examines the SLA associated with the SIOD, our discussion below will not further discuss SSTA.

4. Relative contributions of SIOD and ENSO to Indian Ocean SLA and UOHC

Since the SIOD is correlated with ENSO, with pSIOD being associated with La Niña condition (section 3a), our regression analysis of section 3 includes the effect of ENSO. Indeed, the correlation coefficient between the JFM SDMI and the NDJ Niño-3.4 index with a flipped

sign is 0.36 (>95% significance), and ~40% (5 out of 13) of the observed pSIOD events co-occur with La Niña in observations (Fig. 10). This result suggests that the ENSO forcing may indeed play a role in causing some SIOD events, but the SIOD can also occur independently from ENSO. For the negative SIOD events, four out of eight events are accompanied with El Niño. Below, we focus on examining the pSIOD events, given the smaller sample size of negative SIOD events.

a. Effects of ENSO versus SIOD

By analyzing the lead-lag correlation between ENSO and SIOD-related signals, we find that the maximum correlation between the flipped Niño-3.4 index and the SDMI (the SLA dipole index) occurs when ENSO leads by 2 (3) months (Fig. 11a), with $r_{\max} = 0.25$ (0.55). Hence, we focus on the impact of NDJ ENSO signals on JFM SIOD-associated Indian Ocean variability. As expected, both the JFM SDMI and the NDJ Niño-3.4 index are significantly correlated with the JFM SLA dipole index, with the correlation coefficient being 0.62 and 0.66, respectively (Fig. 11b). To separate the effects of SIOD and ENSO on the SLA and UOHC, we use partial correlation analysis to remove the ENSO influence on the SDMI. The results show that the ENSO-independent SDMI-SLA dipole correlation only drops slightly ($r = 0.54$), suggesting that the SIOD itself is associated with the SLA dipole.

To further assess the contributions of SIOD and ENSO to SLA/D20A in each region of the SLA dipole (i.e., SCTR and southeast of Madagascar), we calculated the correlations between Niño-3.4 index/SDMI and SLA time series averaged over each of the two regions (Fig. 11). Over the SCTR region, both ENSO ($r = -0.72$) and SIOD with ENSO signals included ($r = -0.53$) are closely associated with SLA (Fig. 11b), with ENSO playing a larger role and leading the SLAs by 3 months (Fig. 11a). After removing the ENSO impact, the SIOD is still closely associated with SLA in the region ($r = -0.42$). In the south pole of the dipole southeast of Madagascar, in contrast, SLAs are primarily associated with the SIOD ($r = 0.38$), while the ENSO impact is negligible ($r = 0.05$) (Fig. 11b) and shows no apparent lead-lag correlation with SLA (Fig. 11a). As a result, removing the ENSO impact yields a similar correlation coefficient between the SDMI and SLA index ($r = 0.39$). Hence, although ENSO strongly affects the north pole of the SLA dipole over the SCTR, it is the SIOD that is associated with the SLA dipole.

Spatial patterns of the SLAs associated with the ENSO and ENSO-independent SIOD are also examined.

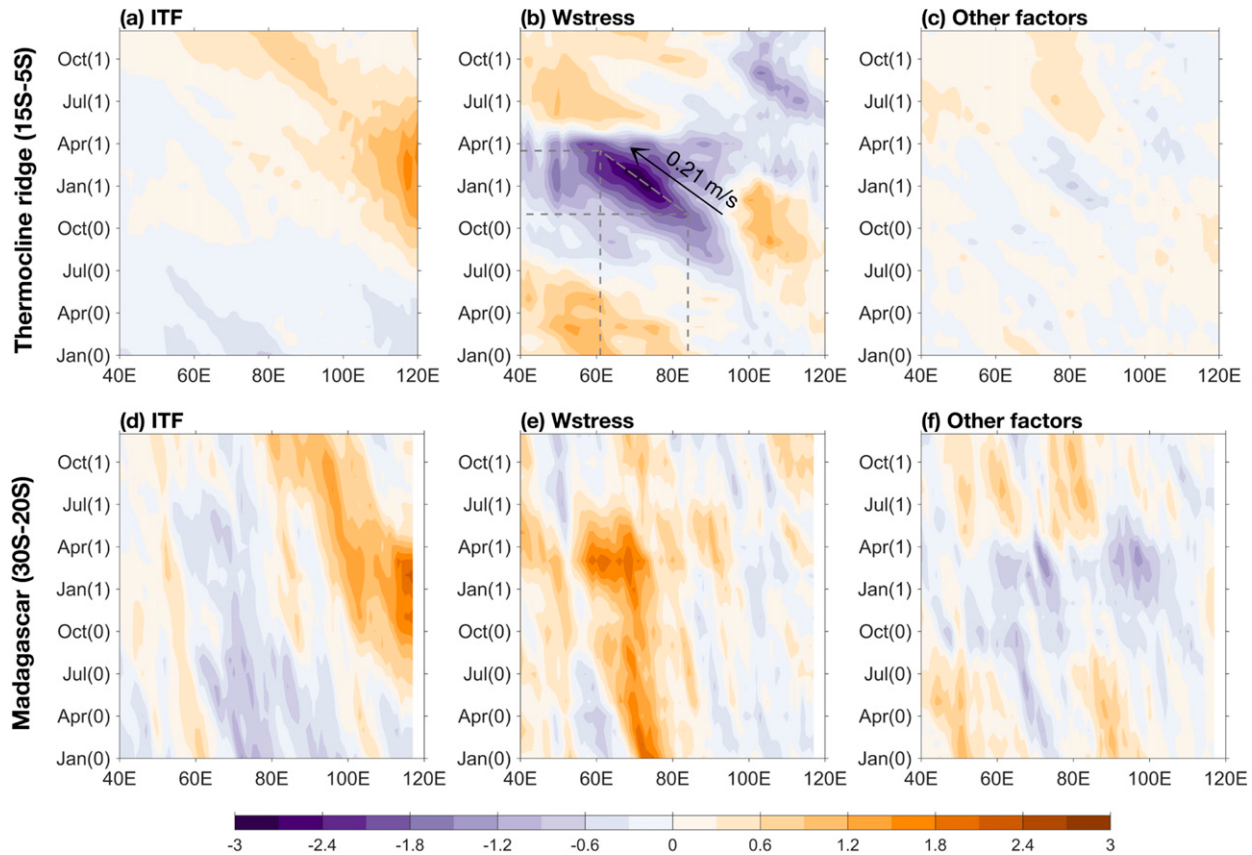


FIG. 9. (a) Lead–lag regression of SLA (shading; cm) in HYCOM_ITF (ITF effect) averaged over the latitudinal band 15° – 5° S on the normalized JFM SDMI in HYCOM_MR. (b) As in (a), but for results in HYCOM_TAU – HYCOM_ITF (surface wind stress effect). The phase speed of oceanic Rossby waves is estimated at approximately 0.21 m s^{-1} . (c) As in (a), but for results in HYCOM_MR – HYCOM_TAU (other factors). (d)–(f) As in (a)–(c), but for SLA averaged over 30° – 20° S.

Linear regression of the JFM Indian Ocean SLA on the NDJ Niño-3.4 index shows that ENSO impacts are significant in the eastern Indian Ocean and the SCTR region (Fig. 12a); the former is associated with the ITF effect, and the latter is caused by the cyclonic wind anomalies in the south tropical Indian Ocean and the subsequent oceanic Rossby waves. In the subtropical (south of 15° S) southwest Indian Ocean, however, ENSO has negligible impacts on SLAs. After removing the ENSO effects from the SLA and wind fields and calculating regression of the residual on the JFM SDMI, we further analyze the pure SIOD impacts (Fig. 12b). The major differences between the SLAs associated with the two climate modes are found in the southwest and eastern Indian Ocean. In the western basin, the SIOD is associated with a prominent north–south SLA dipole, similar to the SLA pattern obtained in our above analysis (e.g., Fig. 1d). Note that in the SCTR region, the SLA associated with ENSO is stronger than with SIOD, suggesting that ENSO is playing a more dominant role in causing SLA in the region. In the eastern Indian

Ocean, cyclonic wind anomalies associated with the SIOD induce negative SLA, which are opposite to the ENSO impacts via the ITF changes with the SIOD effects being much smaller near the Australian west coast. In addition, while ENSO can induce significant wind anomalies in the equatorial and north Indian Ocean, the SIOD has little influence on winds there (Fig. 12). These results suggest that the possible SIOD effect on equatorial winds speculated in Thompson et al. (2016) might result from ENSO, instead of the SIOD.

We have also compared the SLAs during the years when La Niña and pSIDO co-occur and the years when there is only pSIDO based on Fig. 10. Note that the Indian Ocean SLAs in Fig. 12c are associated with the combined effect of La Niña and pSIDO, which exhibit negative SLAs in the SCTR (through the atmospheric bridge) and positive SLAs in the eastern Indian Ocean (through the ITF effect) due to the La Niña forcing, and a north–south dipole-like pattern in the southwest Indian Ocean due to the pSIDO. When there is no La Niña, the SLA in the SCTR region is significantly

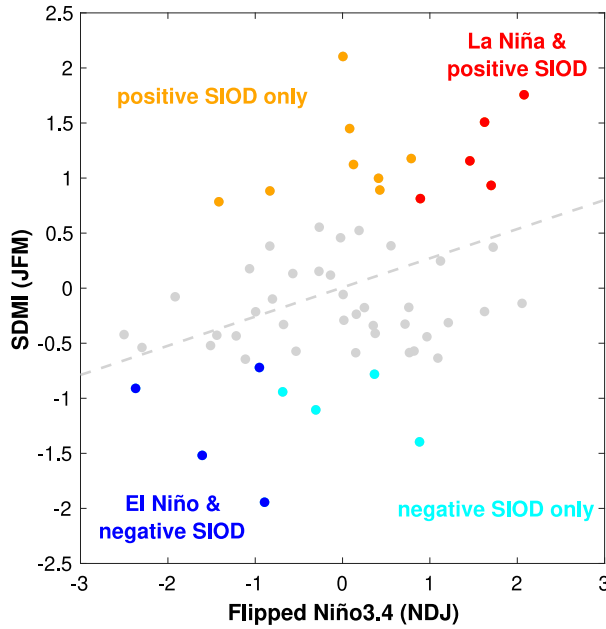


FIG. 10. Scatterplot of the NDJ Niño-3.4 index (flipped sign; °C) and the JFM SDMI (°C). Red and orange (cyan and blue) dots denote positive (negative) SIOD events, which are defined as the year when the JFM SDMI exceeds (falls below negative) one standard deviation. Red dots denote co-occurrence of La Niña and positive SIOD, and orange dots denote positive SIOD only years. Blue dots denote co-occurrence of El Niño and negative SIOD events, and cyan for negative SIOD only years. The selected years are listed in Table S1. The gray dashed line denotes the linear regression of the JFM SDMI on the flipped NDJ Niño-3.4 index.

weakened, but the pSIOD alone is still associated with the SLA dipole (Fig. 12d), which is similar to the linear regression results (Fig. 12b). In the eastern Indian Ocean, the pSIOD is associated with negative SLAs in the absence of La Niña, but its effect is weak or negligible near the Western Australian coast. These results further support that although the SCTR region is strongly affected by ENSO, the independent SIOD is associated with the SLA dipole.

As mentioned earlier, the SLAs associated with SIOD exhibit decadal variations (Fig. 2). After the late 1980s, the SIOD becomes weaker while the ENSO variance exhibits no significant changes (Fig. 2h). As a result, the regression analysis of SLA over the period 1993–2016 is more affected by the remote ENSO impacts, and thus exhibits larger signals in the SCTR region and smaller signals to the southeast of Madagascar (Figs. 2b,d). Prior to the late 1980s, on the other hand, the SIOD is as strong as ENSO, and therefore, the SLA pattern associated with SIOD exhibits an evident dipole structure (Fig. 2f).

Comparing the SSTA patterns during the pSIOD that co-occurred with La Niña years with those of the pSIOD

only years (Figs. 12e,f), it is apparent that the combined effects of pSIOD and La Niña are associated with westward extended and shifted cold pole in the subtropical south Indian Ocean. As a result, the SSTA dipole is more oriented in the north–south direction compared to the SSTA associated with pure SIOD impacts. Off the west coast of Australia, La Niña actually induces weak positive SSTA, which could be due to the enhanced ITF. Previous studies also show that coastal northerly wind anomalies play an important role in causing the SST warming in the southeast Indian Ocean (Feng et al. 2013; Zhang et al. 2018), but the coastal wind anomalies are weak in Fig. 12e. Such a discrepancy could arise from the fact that it is the local air–sea interaction between the coastal SST warming and alongshore wind anomalies that induces prominent changes in SST and wind, while these coastal anomalies are weak in the composite of pSIOD and La Niña because they mainly are associated with signals off the coast.

Influences of La Niña on the SIOD are primarily through the associated cyclonic wind anomalies over the southeast Indian Ocean, which enhances the climatological southeasterly winds at its western flank, increasing surface heat loss, causing cold SSTA, and thus enhancing the cold pole of the SIOD (Fig. 13c). La Niña impacts on the warm SSTA to the southeast of Madagascar, on the other hand, are negligible due to the weak wind response to the ENSO forcing there. Indeed, ENSO is well correlated with the east pole of the SIOD SSTA dipole, with a 2-month time lead, but has little influences on the west pole (Figs. 13a,b). Therefore, the spatial patterns of both SSTA and SLA induced by the SIOD can be quite different from those caused by ENSO forcing.

b. A new index for SIOD

Based on the different SSTA patterns associated with ENSO and SIOD in the south Indian Ocean, we define a new SDMI to eliminate the ENSO effect and better capture the pure SIOD impacts. The new SDMI is defined as the SSTA difference between the western and eastern part of the subtropical south Indian Ocean, which is the SSTA averaged over 55° – 65° E, 37° – 27° S minus that averaged over 105° – 115° E, 37° – 27° S (Fig. 14a). Note that the east pole covers an area in which the ENSO-related SSTA is relatively small, minimizing the ENSO impact on the new index. The new SDMI indeed exhibits some differences from the original index ($r = 0.87$; Fig. 14d), and those discrepancies are attributable to the ENSO forcing, with a correlation coefficient between the flipped Niño-3.4 index and the SDMI difference ~ 0.41 (Fig. 14e).

Regression of SSTA, SLA, and the wind field on the new SDMI clearly shows that the associated Pacific

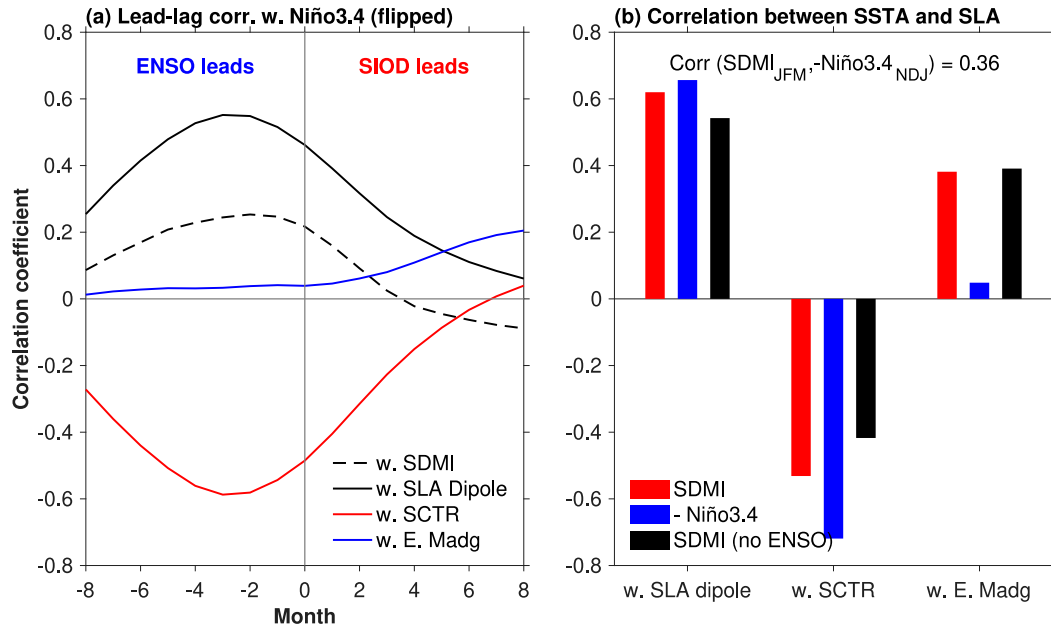


FIG. 11. (a) Lead–lag correlation between the flipped Niño-3.4 index and the SDMI (dashed black line), the SLA dipole (solid black line), SLA at SCTR (solid red line), and SLA to the southeast of Madagascar (solid blue line). Negative values in the x axis denote Niño-3.4 index leading other indices. (b) Correlation coefficients between SSTA and SLA indices. The first column shows correlation with JFM SLA dipole index; the second column shows correlation with JFM SLA at SCTR, and the third column shows correlation with JFM SLA southeast of Madagascar (boxed region in Fig. 1d). Red (blue) shows correlation between JFM SDMI (flipped NDJ Niño-3.4 index) and SLA indices. Black shows partial correlation between JFM SDMI and JFM SLA indices with ENSO impact (NDJ Niño-3.4 index) removed. The correlation coefficient between the JFM SDMI and the flipped NDJ Niño-3.4 index is 0.36.

signals are negligible compared to the previous analysis using the original SDMI (Figs. 1 and 14a,b), while the large-scale features in the subtropical south Indian Ocean, including the SLA dipole, are retained. It is also interesting to note that in Fig. 14b, both the SLAs and SSTAs along the Western Australian coast are negative, indicating that the La Niña-induced positive SLAs and SSTAs through the ITF effect and coastal wind anomalies are largely excluded using the new SDMI index. The air-sea CO₂ flux anomalies associated with the new SDMI exhibit a similar pattern to the SSTA, while the tropical Pacific shows an east–west dipole that is statistically insignificant (Fig. 14c).

Lead–lag correlations show that the correlation between the new SDMI and Niño-3.4 index is weak at both poles, in contrast with the good correlation between the Niño-3.4 index and the east pole of the SSTA dipole using the original SDMI in Behera and Yamagata (2001) (Figs. 13a and 14f). The new SDMI therefore may be more suitable for investigating pure SIOD effects for future studies.

5. Summary and discussion

Upper-ocean variability (e.g., SST, thermocline, and upper-ocean heat content) in the Indian Ocean associated

with the subtropical Indian Ocean dipole (SIOD) is investigated through both observational analysis and HYCOM experiments. It is found that the SIOD is associated with prominent SLAs in the south Indian Ocean, which exhibits a southwest–northeast dipole pattern, with negative SLAs appearing in the Seychelles–Chagos thermocline ridge (SCTR) region (the north pole) and positive SLAs appearing to the southeast of Madagascar (south pole) during positive SIOD (pSIOD) years (Fig. 1d). The SLA dipole pattern is different from the SSTA dipole of the SIOD (Fig. 1c). While the thermocline depth and upper-ocean heat content anomalies mirror SLAs, the CO₂ flux anomalies in the south Indian Ocean are primarily controlled by SSTAs.

The differences between the SLA and SSTA patterns associated with the SIOD are due to different leading physical processes at play. HYCOM experiments suggest that while the SSTAs of the SIOD are mainly caused by surface heat fluxes anomalies associated with large-scale atmospheric conditions, oceanic dynamical processes driven by surface wind stress anomalies over the Indian Ocean play a dominant role in causing the SLA dipole (Fig. 8). The SLAs in the SCTR region result primarily from the westward propagation of oceanic Rossby waves generated by winds to the east, where the

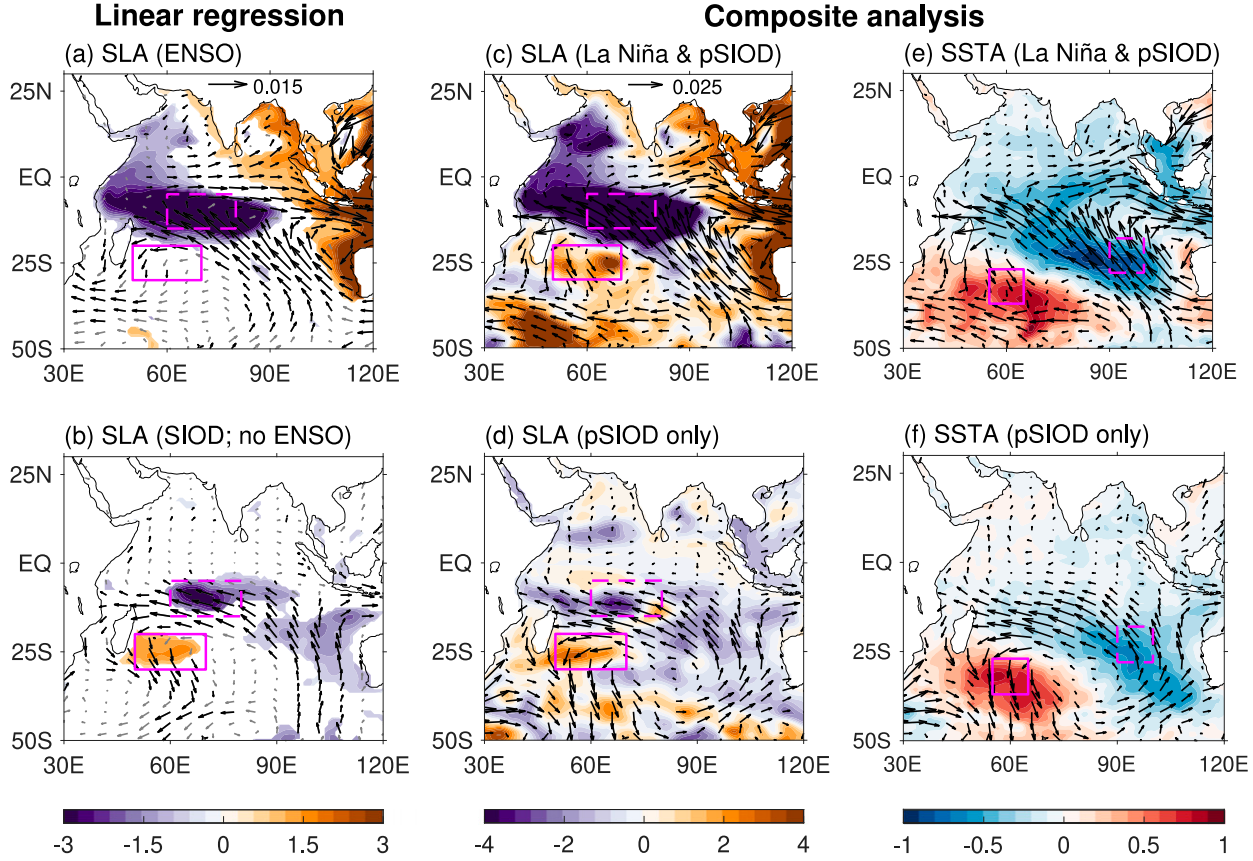


FIG. 12. (a) Regression of JFM SLA (cm) and surface wind stress (N m^{-2}) on the flipped normalized NDJ Niño-3.4 index. (b) As in (a), but for regression on the JFM SDMI, with ENSO impacts removed by removing linear regressions of variables on the NDJ Niño-3.4 index from SLA and surface wind stress fields. (c) Composite of JFM SLA (cm) and surface wind stress anomalies (N m^{-2}) during years when La Niña and positive SIOD co-occur. (d) As in (c), but for composite of positive SIOD only years. See Fig. 10 for selected years. (e),(f) As in (c) and (d), but for composite of JFM SSTA ($^{\circ}\text{C}$) and surface wind stress anomalies. Shading and black vectors in (a) and (b) denote results that are statistically significant at the 90% confidence level. Statistical significance test is not included in (c)–(f) because of the small sample size of the composite analysis.

cyclonic wind stress anomalies cause positive Ekman pumping velocity and thus negative SLAs during pSIOD events (Fig. 4). The SLAs are further enhanced while they propagate westward by wind anomalies along the Rossby waves' characteristics (Fig. 6). The phase speed estimated from the SLA signals falls between the Rossby waves' speeds associated with the first and second baroclinic modes, indicating the importance of the first two modes in contributing to the SLA signals (Fig. 5). Note however that due to local wind forcing and oceanic instabilities, the estimated Rossby wave speed may not accurately represent the theoretically predicted free Rossby wave speed. To the southeast of Madagascar, positive SLAs are mainly caused by local anti-cyclonic wind anomalies during pSIOD, even though westward propagation of Rossby waves can be seen but at a much slower speed because it is located at higher latitude.

Note that the SIOD is partly associated with ENSO forcing, with pSIOD sometimes corresponding to La Niña condition in the tropical Pacific. During our analysis period from 1958 to 2016, about 40% of the observed pSIOD events (5 out of 13) co-occur with La Niña; four out of eight negative SIOD events are accompanied by El Niño (Fig. 10). The association between ENSO and SIOD is primarily through the ENSO impact on the cold pole of the SSTA dipole in the southeast Indian Ocean, since ENSO has little influence on the warm SSTA southeast of Madagascar (Fig. 13). The cyclonic wind anomalies over the southeast Indian Ocean induced by La Niña cause cold SSTA at its western flank, enhancing the cold pole of the pSIOD. It is also interesting to investigate the trigger of the SIOD that is independent of ENSO, such as the southern annular mode (SAM) that could induce zonal wind anomalies over the midlatitude

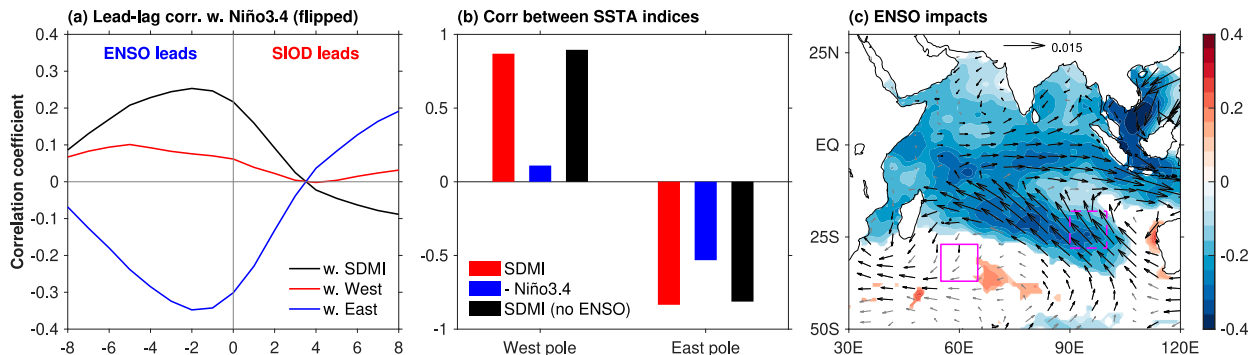


FIG. 13. (a) Lead-lag correlation between the flipped Niño-3.4 index and the SDMI (solid black line), the west pole of the SSTA dipole (solid red line), and the east pole of the SSTA dipole (solid blue line). Negative values in the x axis denote Niño-3.4 index leading other indices. (b) Correlation coefficient between SSTA indices. The first column shows correlation with JFM SSTA averaged over the west pole of the SSTA dipole and the second column the correlation over the east pole (boxed region in Fig. 1c). Red (blue) shows correlation between JFM SDMI (flipped NDJ Niño-3.4 index) and SSTA indices. Black shows partial correlation between JFM SDMI and JFM SSTA indices with ENSO impact (NDJ Niño-3.4 index) removed. (c) Regression of JFM SSTA (cm) and surface wind stress (N m^{-2}) on the flipped normalized NDJ Niño-3.4 index. Shading and black vectors in (c) denote the results that are statistically significant at the 90% confidence level.

south Indian Ocean, but this is beyond the scope of this study.

We find that while ENSO causes significant SLAs in the southeast Indian Ocean via the enhanced ITF and over the SCTR region through exciting Rossby waves by the cyclonic wind anomalies, its impact on the SLAs to the southeast of Madagascar (the south pole of the SLA dipole) is negligible. On the other hand, the SIOD independent of ENSO is associated with opposite SLA in the SCTR and southeast of Madagascar (i.e., the SLA dipole) (Figs. 11 and 12). Hence, although the projection of SIOD on SLAs is generally weaker than that of ENSO, it could still be important for regional climate prediction, particularly for the Mascarene Islands nations where the ENSO impact is negligible.

Given that the original subtropical dipole mode index (SDMI) introduced by Behera and Yamagata (2001) is correlated with ENSO, it is difficult to directly analyze the SIOD impacts using that index without removing the ENSO effect. Here, we propose a new SDMI using SSTA differences between the western and eastern subtropical south Indian Ocean where the ENSO influences are small (Fig. 14). This new index is uncorrelated with ENSO, yet still captures the large-scale SLA and SSTA features associated with the SIOD well. Therefore, it could be readily used to extract the large-scale anomalies associated with the SIOD, while minimizing the ENSO impacts. For instance, we find that the regression of precipitation on the new SDMI exhibits prominent south-central African rainfall anomalies (Fig. S3), which supports the finding that the SIOD is associated with rainfall anomalies over Africa (Behera

and Yamagata 2001). However, the new SDMI does not necessarily suggest total independence of the SIOD from ENSO. If one defines the SIOD as a northeast-southwest SSTA dipole in the subtropical south Indian Ocean, ENSO could still excite or contribute to some SIOD events, with some SIOD events occurring independently.

Results presented in this study show that SIOD is indeed associated with evident SLA and upper-ocean variability (thermocline depth and heat content) in the south Indian Ocean on interannual time scales, but with significant decadal variations. This may help explain and resolve the relatively small explained variance of SLAs in the subtropical south Indian Ocean when the SIOD effect is not considered (Frankcombe et al. 2015). Consequently, future sea level predictions in the south Indian Ocean need to consider the SIOD impacts, particularly when the SIOD occurs without ENSO, which can have large influence on sea level variability over the Seychelles–Chagos and Mascarene Islands nations. In addition, because of the small sample size due to the short observational period available for analysis, it is difficult to accurately disentangle the impact of the SIOD from that of ENSO. A future study targeting the mechanisms of SIOD-related SLAs in a larger sample size by analyzing large ensemble climate model experiments is warranted.

Acknowledgments. The work is supported by NASA Ocean Surface Topography Science Team NNX17AI63G, NASA Physical Oceanography Program NNX17AH25G, and NSF OCE 1658132. NSL is grateful for funding from NSF (OCE-1752724,

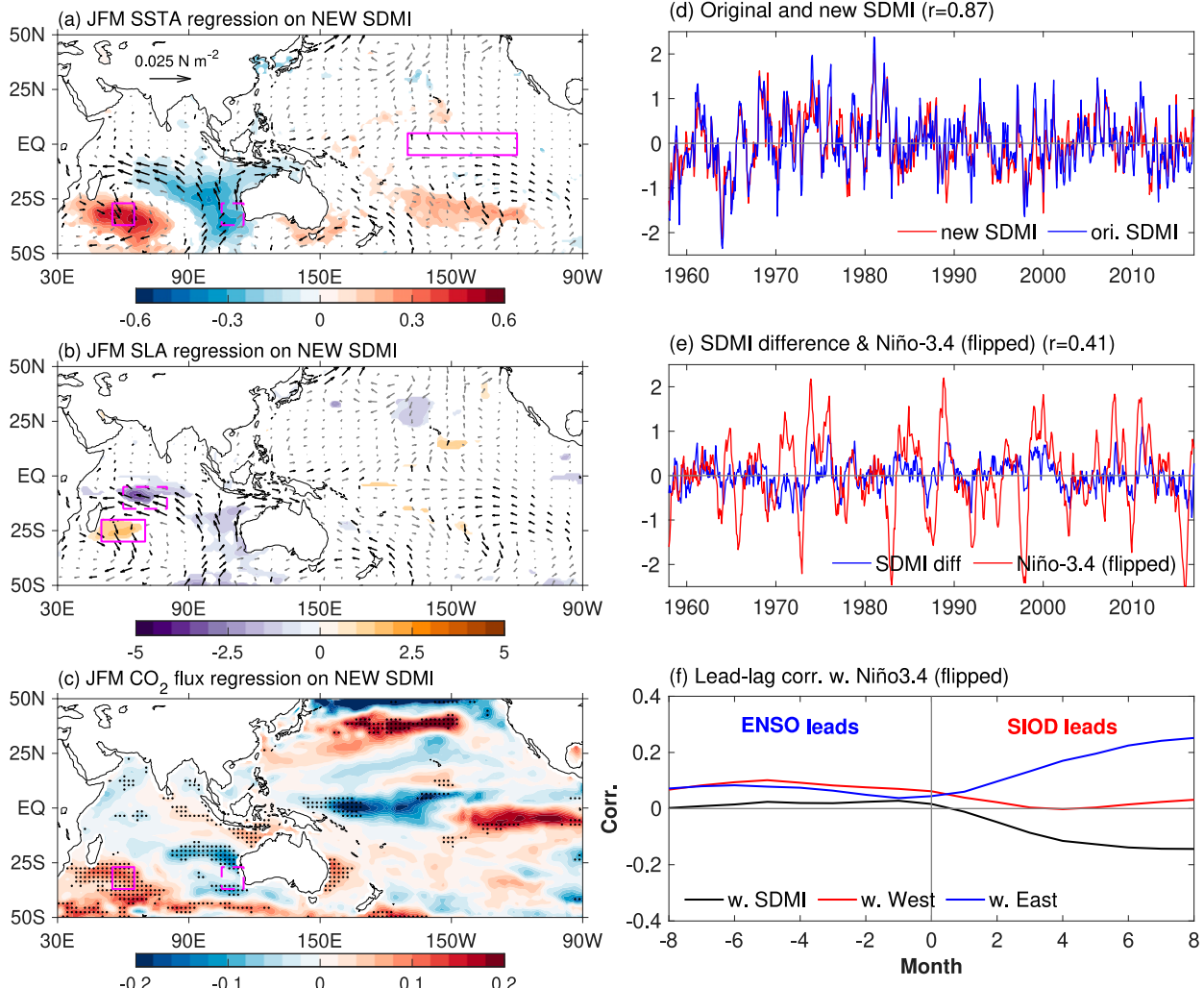


FIG. 14. (a) Regression of JFM SST ($^{\circ}$ C) and surface wind stress anomalies ($N m^{-2}$) on the new SDMI, which is defined as differences of SST averaged over 55° – 65° E, 37° – 27° S and 105° – 115° E, 37° – 27° S [boxed region in (a)]. (b),(c) As in (a), but for regression of JFM SLA (cm) and CO₂ flux density anomalies ($mol m^{-2} yr^{-1}$). Shading and black vectors in (a) and (b) and stippling in (c) denote results that are statistically significant at the 90% confidence level. (d) Time evolution of the new SDMI (red) and the SDMI from Behera and Yamagata (2001) (blue). The correlation coefficient between the two is 0.87. (e) Difference of the two SDMIs in (d) (original SDMI minus new SDMI; blue) and the flipped Niño-3.4 index (red); their correlation coefficient is 0.41. (f) Lead-lag correlation between the flipped Niño-3.4 index and the new SDMI (solid black line), the west pole of the SST dipole (solid red line), and the east pole of the SST dipole (solid blue line). Negative values in the x axis denote the Niño-3.4 index leading other indices.

OCE-1558225). We also thank NCAR CISL for their computational support for the HYCOM simulations.

REFERENCES

- Balmaseda, M. A., K. Mogensen, and A. T. Weaver, 2013a: Evaluation of the ECMWF ocean reanalysis system ORAS4. *Quart. J. Roy. Meteor. Soc.*, **139**, 1132–1161, <https://doi.org/10.1002/qj.2063>.
- , K. E. Trenberth, and E. Källén, 2013b: Distinctive climate signals in reanalysis of global ocean heat content. *Geophys. Res. Lett.*, **40**, 1754–1759, <https://doi.org/10.1002/grl.50382>.
- Bates, N. R., A. C. Pequignet, and C. L. Sabine, 2006: Ocean carbon cycling in the Indian Ocean: 1. Spatiotemporal variability of inorganic carbon and air-sea CO₂ gas exchange. *Global Biogeochem. Cycles*, **20**, GB3020, <https://doi.org/10.1029/2005GB02491>.
- Behera, S. K., and T. Yamagata, 2001: Subtropical SST dipole events in the southern Indian Ocean. *Geophys. Res. Lett.*, **28**, 327–330, <https://doi.org/10.1029/2000GL011451>.
- Bjerknes, J., 1969: Atmospheric teleconnections from the equatorial Pacific. *Mon. Wea. Rev.*, **97**, 163–172, [https://doi.org/10.1175/1520-0493\(1969\)097<0163:ATFTEP>2.3.CO;2](https://doi.org/10.1175/1520-0493(1969)097<0163:ATFTEP>2.3.CO;2).
- Bleck, R., 2002: An oceanic general circulation model framed in hybrid isopycnic-Cartesian coordinates. *Ocean Modell.*, **4**, 55–88, [https://doi.org/10.1016/S1463-5003\(01\)00012-9](https://doi.org/10.1016/S1463-5003(01)00012-9).

- Cane, M. A., S. E. Zebiak, and S. C. Dolan, 1986: Experimental forecasts of El Niño. *Nature*, **321**, 827–832, <https://doi.org/10.1038/321827a0>.
- Chambers, D. P., B. D. Tapley, and R. H. Stewart, 1999: Anomalous warming in the Indian Ocean coincident with El Niño. *J. Geophys. Res.*, **104**, 3035–3047, <https://doi.org/10.1029/1998JC000085>.
- Chioldi, A. M., and D. E. Harrison, 2007: Mechanisms of summertime subtropical southern Indian Ocean sea surface temperature variability: On the importance of humidity anomalies and the meridional advection of water vapor. *J. Climate*, **20**, 4835–4852, <https://doi.org/10.1175/JCLI4271.1>.
- Clarke, A. J., and X. Liu, 1994: Interannual sea level in the northern and eastern Indian Ocean. *J. Phys. Oceanogr.*, **24**, 1224–1235, [https://doi.org/10.1175/1520-0485\(1994\)024<1224:ISLTIN>2.0.CO;2](https://doi.org/10.1175/1520-0485(1994)024<1224:ISLTIN>2.0.CO;2).
- , —, and J. Li, 2004: El Niño/La Niña shelf edge flow and Australian western rock lobsters. *Geophys. Res. Lett.*, **31**, L11301, <https://doi.org/10.1029/2003GL018900>.
- Dee, D. P., and Coauthors, 2011: The ERA-Interim reanalysis: Configuration and performance of the data assimilation system. *Quart. J. Roy. Meteor. Soc.*, **137**, 553–597, <https://doi.org/10.1002/qj.828>.
- Deepa, J. S., C. Gnanaseelan, R. Kakatkar, A. Parekh, and J. S. Chowdary, 2018: The interannual sea level variability in the Indian Ocean as simulated by an ocean general circulation model. *Int. J. Climatol.*, **38**, 1132–1144, <https://doi.org/10.1002/joc.5228>.
- , —, S. Mohapatra, J. S. Chowdary, A. Karmakar, R. Kakatkar, and A. Parekh, 2019: The tropical Indian Ocean decadal sea level response to the Pacific decadal oscillation forcing. *Climate Dyn.*, **52**, 5045–5085, <https://doi.org/10.1007/s00382-018-4431-9>.
- Ducet, N., P. Y. Le Traon, and G. Reverdin, 2000: Global high-resolution mapping of ocean circulation from TOPEX/Poseidon and ERS-1 and -2. *J. Geophys. Res.*, **105**, 19 477–19 498, <https://doi.org/10.1029/2000JC000063>.
- Feng, M., G. Meyers, and S. Wijffels, 2001: Interannual upper ocean variability in the tropical Indian Ocean. *Geophys. Res. Lett.*, **28**, 4151–4154, <https://doi.org/10.1029/2001GL013475>.
- , Y. Li, and G. Meyers, 2004: Multidecadal variations of Fremantle sea level: Footprint of climate variability in the tropical Pacific. *Geophys. Res. Lett.*, **31**, L16302, <https://doi.org/10.1029/2004GL019947>.
- , M. J. McPhaden, S.-P. Xie, and J. Hafner, 2013: La Niña forces unprecedented Leeuwin Current warming in 2011. *Sci. Rep.*, **3**, 1277, <https://doi.org/10.1038/SREP01277>.
- Frankcombe, L. M., S. McGregor, and M. H. England, 2015: Robustness of the modes of Indo-Pacific sea level variability. *Climate Dyn.*, **45**, 1281–1298, <https://doi.org/10.1007/s00382-014-2377-0>.
- Fukumori, I., R. Raghunath, and L.-L. Fu, 1998: Nature of global large-scale sea level variability in relation to atmospheric forcing: A modeling study. *J. Geophys. Res.*, **103**, 5493–5512, <https://doi.org/10.1029/97JC02907>.
- Gill, A. E., 1980: Some simple solutions for heat-induced tropical circulation. *Quart. J. Roy. Meteor. Soc.*, **106**, 447–462, <https://doi.org/10.1002/qj.49710644905>.
- Gualdi, S., E. Guilyardi, A. Navarra, S. Masina, and P. Delecluse, 2003: The interannual variability in the tropical Indian Ocean as simulated by a CGCM. *Climate Dyn.*, **20**, 567–582, <https://doi.org/10.1007/s00382-002-0295-z>.
- Han, W., G. A. Meehl, and A. Hu, 2006: Interpretation of tropical thermocline cooling in the Indian and Pacific Oceans during recent decades. *Geophys. Res. Lett.*, **33**, L23615, <https://doi.org/10.1029/2006GL027982>.
- , —, and Coauthors, 2014: Indian Ocean decadal variability: A review. *Bull. Amer. Meteor. Soc.*, **95**, 1679–1703, <https://doi.org/10.1175/BAMS-D-13-00028.1>.
- , G. A. Meehl, D. Stammer, A. Hu, B. Hamlington, J. Kenigson, H. Palanisamy, and P. Thompson, 2017: Spatial patterns of sea level variability associated with natural internal climate modes. *Surv. Geophys.*, **38**, 217–250, <https://doi.org/10.1007/s10712-016-9386-y>.
- , D. Stammer, G. Meehl, A. Hu, F. Sienz, and L. Zhang, 2018: Multi-decadal trend and decadal variability of the regional sea level over the Indian Ocean since the 1960s: Roles of climate modes and external forcing. *Climate*, **6**, 51, <https://doi.org/10.3390/cli6020051>.
- , —, P. Thompson, T. Ezer, H. Palanisamy, X. Zhang, C. M. Domingues, L. Zhang, and D. Yuan, 2019: Impacts of basin-scale climate modes on coastal sea level: A review. *Surv. Geophys.*, <https://doi.org/10.1007/s10712-019-09562-8>.
- Hermes, J. C., and C. J. C. Reason, 2005: Ocean model diagnosis of interannual coevolving SST Variability in the South Indian and South Atlantic Oceans. *J. Climate*, **18**, 2864–2882, <https://doi.org/10.1175/JCLI3422.1>.
- Huang, B., and J. L. Kinter III, 2002: Interannual variability in the tropical Indian Ocean. *J. Geophys. Res.*, **107**, 3199, <https://doi.org/10.1029/2001JC001278>.
- Iizuka, S., T. Matsuura, and T. Yamagata, 2000: The Indian Ocean SST dipole simulated in a coupled general circulation model. *Geophys. Res. Lett.*, **27**, 3369–3372, <https://doi.org/10.1029/2000GL011484>.
- Kopp, R. E., C. C. Hay, C. M. Little, and J. X. Mitrovica, 2015: Geographic variability of sea-level change. *Curr. Climate Change Rep.*, **1**, 192–204, <https://doi.org/10.1007/s40641-015-0015-5>.
- Landschützer, P., N. Gruber, D. C. Bakker, and U. Schuster, 2014: Recent variability of the global ocean carbon sink. *Global Biogeochem. Cycles*, **28**, 927–949, <https://doi.org/10.1002/2014GB004853>.
- Li, Y., and W. Han, 2015: Decadal sea level variations in the Indian Ocean investigated with HYCOM: Roles of climate modes, ocean internal variability, and stochastic wind forcing. *J. Climate*, **28**, 9143–9165, <https://doi.org/10.1175/JCLI-D-15-0252.1>.
- , —, and L. Zhang, 2017: Enhanced decadal warming of the southeast Indian Ocean during the recent global surface warming slowdown. *Geophys. Res. Lett.*, **44**, 9876–9884, <https://doi.org/10.1002/2017GL075050>.
- , —, A. Hu, G. A. Meehl, and F. Wang, 2018: Multidecadal changes of the upper Indian Ocean heat content during 1965–2016. *J. Climate*, **31**, 7863–7884, <https://doi.org/10.1175/JCLI-D-18-0116.1>.
- Llovel, W., and T. Lee, 2015: Importance and origin of halosteric contribution to sea level change in the southeast Indian Ocean during 2005–2013. *Geophys. Res. Lett.*, **42**, 1148–1157, <https://doi.org/10.1002/2014GL062611>.
- Masumoto, Y., and G. Meyers, 1998: Forced Rossby waves in the southern tropical Indian Ocean. *J. Geophys. Res.*, **103**, 27 589–27 602, <https://doi.org/10.1029/98JC02546>.
- Metzl, N., A. Poisson, F. Louanchi, C. Brunet, B. Schauer, and B. Bres, 1995: Spatio-temporal distributions of air-sea fluxes of CO₂ in the Indian and Antarctic Oceans. *Tellus*, **47B**, 56–69, <https://doi.org/10.3402/tellusb.v47i1-2.16006>.
- Meyers, G., 1996: Variation of Indonesian throughflow and the El Niño–Southern Oscillation. *J. Geophys. Res.*, **101**, 12 255–12 263, <https://doi.org/10.1029/95JC03729>.

- Morioka, Y., T. Tozuka, and T. Yamagata, 2010: Climate variability in the southern Indian Ocean as revealed by self-organizing maps. *Climate Dyn.*, **35**, 1059–1072, <https://doi.org/10.1007/s00382-010-0843-x>.
- Nidheesh, A. G., M. Lengaigne, J. Vialard, T. Izumo, A. S. Unnikrishnan, B. Meyssignac, B. Hamlington, and C. de Boyer Montégut, 2017: Robustness of observation-based decadal sea level variability in the Indo-Pacific Ocean. *Geophys. Res. Lett.*, **44**, 7391–7400, <https://doi.org/10.1002/2017GL073955>.
- Philander, S. G., 1990: *El Niño, La Niña, and the Southern Oscillation*. Elsevier, 293 pp.
- Poisson, A., N. Metzl, C. Brunet, B. Schauer, B. Bres, D. Ruiz-Pino, and F. Louanchi, 1993: Variability of sources and sinks of CO₂ in the western Indian and southern oceans during the year 1991. *J. Geophys. Res.*, **98**, 22 759–22 778, <https://doi.org/10.1029/93JC02501>.
- Poli, P., and Coauthors, 2016: ERA-20C: An atmospheric reanalysis of the twentieth century. *J. Climate*, **29**, 4083–4097, <https://doi.org/10.1175/JCLI-D-15-0556.1>.
- Rao, S. A., S. K. Behera, Y. Masumoto, and T. Yamagata, 2002: Interannual subsurface variability in the tropical Indian Ocean with a special emphasis on the Indian Ocean dipole. *Deep-Sea Res. II*, **49**, 1549–1572, [https://doi.org/10.1016/S0967-0645\(01\)00158-8](https://doi.org/10.1016/S0967-0645(01)00158-8).
- Rayner, N. A., D. E. Parker, E. B. Horton, C. K. Folland, L. V. Alexander, D. P. Rowell, E. C. Kent, and A. Kaplan, 2003: Global analyses of sea surface temperature, sea ice, and night marine air temperature since the late nineteenth century. *J. Geophys. Res.*, **108**, 4407, <https://doi.org/10.1029/2002JD002670>.
- Reynolds, R. W., N. A. Rayner, T. M. Smith, D. C. Stokes, and W. Wang, 2002: An improved in situ and satellite SST analysis for climate. *J. Climate*, **15**, 1609–1625, [https://doi.org/10.1175/1520-0442\(2002\)015<1609:AIISAS>2.0.CO;2](https://doi.org/10.1175/1520-0442(2002)015<1609:AIISAS>2.0.CO;2).
- Sabine, C. L., R. Wanninkhof, R. M. Key, C. Goyet, and F. J. Millero, 2000: Seasonal CO₂ fluxes in the tropical and subtropical Indian Ocean. *Mar. Chem.*, **72**, 33–53, [https://doi.org/10.1016/S0304-4203\(00\)00064-5](https://doi.org/10.1016/S0304-4203(00)00064-5).
- Saji, N. H., and T. Yamagata, 2003: Possible impacts of Indian Ocean Dipole mode events on global climate. *Climate Res.*, **25**, 151–169, <https://doi.org/10.3354/cr025151>.
- , B. N. Goswami, P. N. Vinayachandran, and T. Yamagata, 1999: A dipole mode in the tropical Indian Ocean. *Nature*, **401**, 360–363, <https://doi.org/10.1038/43854>.
- Sayantani, O., and C. Gnanaseelan, 2015: Tropical Indian Ocean subsurface temperature variability and the forcing mechanisms. *Climate Dyn.*, **44**, 2447–2462, <https://doi.org/10.1007/s00382-014-2379-y>.
- Shinoda, T., M. A. Alexander, and H. H. Hendon, 2004: Remote response of the Indian Ocean to interannual SST variations in the tropical Pacific. *J. Climate*, **17**, 362–372, [https://doi.org/10.1175/1520-0442\(2004\)017<0362:RROTIO>2.0.CO;2](https://doi.org/10.1175/1520-0442(2004)017<0362:RROTIO>2.0.CO;2).
- Stammer, D., A. Cazenave, R. M. Ponte, and M. E. Tamisiea, 2013: Causes for contemporary regional sea level changes. *Annu. Rev. Mar. Sci.*, **5**, 21–46, <https://doi.org/10.1146/annurev-marine-121211-172406>.
- Suzuki, R., S. K. Behera, S. Iizuka, and T. Yamagata, 2004: Indian Ocean subtropical dipole simulated using a coupled general circulation model. *J. Geophys. Res.*, **109**, C09001, <https://doi.org/10.1029/2003JC001974>.
- Thompson, P. R., C. G. Piecuch, M. A. Merrifield, J. P. McCreary, and E. Firing, 2016: Forcing of recent decadal variability in the equatorial and North Indian Ocean. *J. Geophys. Res. Oceans*, **121**, 6762–6778, <https://doi.org/10.1002/2016JC012132>.
- Tozuka, T., T. Yokoi, and T. Yamagata, 2010: A modeling study of interannual variations of the Seychelles Dome. *J. Geophys. Res.*, **115**, C04005, <https://doi.org/10.1029/2009JC005547>.
- Trenary, L. L., and W. Han, 2008: Causes of decadal subsurface cooling in the tropical Indian Ocean during 1961–2000. *Geophys. Res. Lett.*, **35**, L17602, <https://doi.org/10.1029/2008GL034687>.
- , and —, 2012: Intraseasonal-to-interannual variability of South Indian Ocean sea level and thermocline: Remote versus local forcing. *J. Phys. Oceanogr.*, **42**, 602–627, <https://doi.org/10.1175/JPO-D-11-084.1>.
- , and —, 2013: Local and remote forcing of decadal sea level and thermocline depth variability in the South Indian Ocean. *J. Geophys. Res. Oceans*, **118**, 381–398, <https://doi.org/10.1029/2012JC008317>.
- Webster, P. J., A. M. Moore, J. P. Loschnigg, and R. R. Leben, 1999: Coupled ocean–atmosphere dynamics in the Indian Ocean during 1997–98. *Nature*, **401**, 356–360, <https://doi.org/10.1038/43848>.
- Wijffels, S., and G. Meyers, 2004: An intersection of oceanic waveguides: Variability in the Indonesian Throughflow region. *J. Phys. Oceanogr.*, **34**, 1232–1253, [https://doi.org/10.1175/1520-0485\(2004\)034<1232:AIOOWV>2.0.CO;2](https://doi.org/10.1175/1520-0485(2004)034<1232:AIOOWV>2.0.CO;2).
- Xie, S.-P., H. Annamalai, F. A. Schott, and J. P. McCreary Jr., 2002: Structure and mechanisms of South Indian Ocean climate variability. *J. Climate*, **15**, 864–878, [https://doi.org/10.1175/1520-0442\(2002\)015<0864:SAMOSI>2.0.CO;2](https://doi.org/10.1175/1520-0442(2002)015<0864:SAMOSI>2.0.CO;2).
- Yang, Y., S.-P. Xie, L. Wu, Y. Kosaka, N.-C. Lau, and G. A. Vecchi, 2015: Seasonality and predictability of the Indian Ocean dipole mode: ENSO forcing and internal variability. *J. Climate*, **28**, 8021–8036, <https://doi.org/10.1175/JCLI-D-15-0078.1>.
- Zhang, L., and W. Han, 2018: Impact of Ningaloo Niño on tropical Pacific and an inter-basin coupling mechanism. *Geophys. Res. Lett.*, **45**, 11 300–11 309, <https://doi.org/10.1029/2018GL078579>.
- , —, Y. Li, and T. Shinoda, 2018: Mechanisms for generation and development of Ningaloo Niño. *J. Climate*, **31**, 9239–9259, <https://doi.org/10.1175/JCLI-D-18-0175.1>.
- Zhuang, W., M. Feng, Y. Du, A. Schiller, and D. Wang, 2013: Low-frequency sea level variability in the southern Indian Ocean and its impacts on the oceanic meridional transports. *J. Geophys. Res. Oceans*, **118**, 1302–1315, <https://doi.org/10.1002/jgrc.20129>.

Copyright of Journal of Climate is the property of American Meteorological Society and its content may not be copied or emailed to multiple sites or posted to a listserv without the copyright holder's express written permission. However, users may print, download, or email articles for individual use.